Modified shallow water model for viscous fluids and positivity preserving numerical approximation

Elisa Biagioli[a,*], Mattia de' Michieli Vitturi[b], Fabio Di Benedetto[a,1]

[a]*Department of Mathematics, University of Genoa, Via Dodecaneso 35, 16146 Genova, Italy*
[b]*National Institute of Geophysics and Volcanology INGV, Via Della Faggiola 32, I-56126 Pisa, Italy*

Abstract

Shallow water equations are widely used for the simulation of those geophysical flows for which the flow horizontal length scale is much greater than the vertical one. Inspired by the example of lava flows, we consider here a modified model with an additional transport equation for a scalar quantity (e.g., temperature), and the derivation of the shallow water equations from depth-averaging the Navier-Stokes equations is presented. The assumption of constant vertical profiles for some of the model variables is relaxed allowing the presence of vertical profiles, and it follows that the non-linearity of the flux terms results in the introduction of appropriate shape coefficients.

The space discretization of the resulting system of hyperbolic partial differential equations is obtained with a modified version of the finite volume central-upwind scheme introduced by Kurganov and Petrova in 2007. The time discretization is based on an implicit-explicit Runge-Kutta method which couples properly the hyperbolic part and the stiff source terms, avoiding the use of a very small time step; the use of complex arithmetic increases accuracy in the implicit treatment of stiff terms. The whole scheme is proved to preserve the positivity of flow thickness and the stationary steady-states.

Some numerical experiments are performed to validate the proposed method and to show the incidence on the numerical solutions of shape coefficients introduced in the model.

Keywords: Shallow water equations, viscous fluids, finite volume, numerical scheme, well-balanced, topography.

Introduction

In the past two centuries the shallow water equations, a depth-averaged system of partial differential equations describing the dynamics of inviscid and constant-density fluids for which the flow horizontal length scale is much greater than the vertical one, have been

---

*Corresponding author.
Email addresses: `biagioli@dima.unige.it` (Elisa Biagioli), `mattia.demichielivitturi@ingv.it` (Mattia de' Michieli Vitturi), `dibenede@dima.unige.it` (Fabio Di Benedetto)
[1]Member of Research Group GNCS-INDAM.

widely used for the simulation of a multitude of geophysical flows. In the volcanologic field, for example, they have been applied with success to the simulation of pyroclastic density currents [1], lava flows [2, 3], and lahars [4]. In the meteorological field they are used, with an additional term modeling Coriolis forces, to describe the horizontal structure of the atmosphere [5, 6]; in the study of ocean circulation they are employed to produce global, realistic tidal models [7], and they accurately describe the propagation of a tsunami until waves approach the shore [8, 9].

The classical shallow water equations, first introduced by De Saint Venant in 1864 and Boussinesq in 1872, are based on several assumptions, among which the fact that the vertical pressure distribution is hydrostatic, the vertical component of the velocity can be neglected, and that the horizontal velocity field can be considered constant with depth. In the past, several modifications have been proposed to weaken this last assumption and better model flows where vertical shear is important, resulting in a modified momentum equation where a multiplying coefficient, named *shape* or *Boussinesq factor*, is introduced in the advective flux term [10]. Its magnitude relates the mean square velocity to the square of the mean velocity and reflects the shear in the profile of the horizontal fluid velocity, and may depend on factors such as the Reynolds number or the boundary roughness. It is well known that these modifications do not change the hyperbolic nature of the equations but in some case they can significantly impact the front features and propagation [11].

From the modeling point of view, in this contribution we go a step further, proposing a depth-averaged model for laminar, viscous and incompressible fluids, enriched by a parameter describing the vertical variation of the velocity field (the Boussinesq coefficient) and with an additional transport equation for a scalar quantity varying horizontally and with a non-constant vertical profile. This is the case, for example, of temperature in single phase flows, where a thermal boundary layer develops when fluids flow over a solid, but it is also the case of particle concentration in sediment-laden flows, where a high-concentration basal layer may affect the transport dynamics. Also for this quantity, as done for the velocity field, a shape coefficient describing the vertical profile is introduced, and the resulting depth-averaged transport equation is derived. In addition, we also consider the case where density depends on the depth-averaged temperature, therefore density varies horizontally, further relaxing the assumptions of the classical shallow water equations. The paper illustrates the derivation details of the depth-averaged system of equations from the Navier-Stokes equations; moreover, the hyperbolicity of the system is also studied highlighting the role of the shape parameters.

Due to the non-linearities present in shallow water equations, it is possible to find analytical solutions only in particular cases, and in general a numerical approach is adopted for their solution. When dealing with the numerical solution of depth-averaged flow models, an important issue is the proper tracking of wet/dry fronts, i.e. the propagation of interfaces between regions occupied by the flow (wet) and regions without flow (dry). A large number of numerical models solving for the shallow water equations are based on explicit finite volume schemes [12, 13, 9], and they adopt different strategies to deal with wetting and drying. It is important to remark that the stability of any explicit scheme is controlled by the Courant-Friedrichs-Lewy (CFL) condition and by the maximum characteristic speed

of the governing equations, which depends on the square root of flow thickness. For this reason, a numerical scheme producing negative thickness is not only physically unrealistic, but also results in numerical problems. A simple but effective method to capture wet/dry fronts and to overcome these problems would be set to zero any negative thickness produced by a numerical scheme, together with the corresponding velocities [14], but we observe that this approach does not preserve the total mass of the system. In Godunov-type schemes, other conservative methods have been proposed to treat wetting and drying [15, 16]. A different approach, based on the central-upwind finite-volume scheme, was proposed by Kurganov and Levy (2002) [13] and then adopted in other works [17, 18, 19]. Such different approach on one hand guarantees the positivity of the solution, and on the other hand is able to capture steady states over a complex topography, like those represented by a null velocity and a flat free surface. In literature, methods able to preserve these stationary states are generally called well-balanced methods [20]. In addition to the numerical issues described above, computational instabilities may also arise in the numerical simulation of wet/dry fronts, when friction terms inversely proportional to flow thickness are considered, like for example in the Manning formulation [21]. For this reason it is important to employ appropriate numerical schemes, such as semi-implicit schemes [14, 15], or implicit-explicit Runge-Kutta methods [22, 23].

In this work, we propose a combination of some of the above-mentioned existing techniques. The spatial discretization is performed through a modified version of the central-upwind finite volume scheme introduced by Kurganov and Petrova (2007) [17] for the classical shallow water equations: we adapt the method to our depth-averaged modified model, proving in §2.1 that important properties like well-balancing and positivity preserving for near-dry states are satisfied. We couple this approach with an implicit-explicit Runge-Kutta technique employed to the temporal discretization [23], where a suitable selection of the stiff terms to be treated implicitly is performed in §2.2. A clever use of complex arithmetic, borrowed from [24] and described in §2.2.1, ensures an accurate computation of Jacobians which is necessary for the efficient solution of the implicit part of the scheme.

This combination of choices appears quite efficient: the conservative and positivity-preserving explicit central-upwind numerical scheme allows for a robust and accurate tracking of flow fronts, whereas the implicit treatment of nonlinear viscous terms allows us to properly simulate steady-state equilibrium states and flow stopping conditions, without the need for any ad-hoc empirical criteria.

The outline of the paper is as follows. In §1, the physical model with the derivation of the governing equations and the study of their hyperbolicity are presented. In §2, the numerical model is introduced, describing the spatial and temporal discretizations. In §3, the model is applied to several 1D and 2D cases, where the accuracy of the numerical schemes is studied and where it is shown the effect of the shape factors. The concluding remarks are presented in §4.

1. The physical model

In this section, we present the derivation of a depth-averaged model for the dynamics of an incompressible, laminar, viscous and homogeneous fluid over a variable topography, which takes into account also the transport of an additional quantity with a vertical distribution. This is a quite common feature in environmental science where, for example, this quantity may represent the concentration of sediments [25] or pollutants [26] or in geophysics and volcanological applications, where it may represent the fraction of solid particles in pyroclastic flows [27] or the temperature in lava flows [2], or it may represent both the temperature and the salinity of water in oceanology [28].

Even though it is common to derive depth-averaged equations directly from first principles (conservation of mass and conservation of momentum), here we obtain them from more general transient and 3D fluid equations. Considering a Eulerian framework, the desired equations are in fact derived from the depth-averaging of the Navier-Stokes equations, under the assumption that the horizontal length scale is much greater than the vertical length scale.

For a viscous fluid, ignoring the energy equation, the full 3D conservation of mass and conservation of linear momentum equations (the Navier-Stokes equations) write respectively as

$$\frac{\partial \rho}{\partial t} + \nabla \cdot (\rho \mathbf{u}) = 0, \tag{1}$$

$$\frac{\partial (\rho \mathbf{u})}{\partial t} + \nabla \cdot \left(\rho \mathbf{u} \mathbf{u}^T \right) = -\nabla p - \nabla \cdot \tau, \tag{2}$$

where $\rho(x, y, z, t)$ is the fluid density, $\mathbf{u}(x, y, z, t)$ is the velocity vector field (with components (u, v, w)), $p = p(x, y, z, t)$ is the pressure and $\tau = \tau(x, y, z, t)$ is the viscous term. In the case of a Newtonian and incompressible fluid, the viscous term reduces to

$$\tau = \mu(\nabla \mathbf{u} + (\nabla \mathbf{u})^T), \tag{3}$$

with μ being the dynamic viscosity. Viscosity is intrinsically related to the physical nature and chemical composition of involved materials, and it may vary according to other factors involved into the event dynamics. For example, such factors might be the crystal fraction (as in the celebrated Krieger-Dougherty equation [29]) or the quantity of bubbles for a magmatic fluid, but also the temperature (for example in the Arrhenius model for liquid or the Costa and Macedonio [2] lava model) or the concentration of sediments for other geophysical flows.

Even though we are interested in incompressible flows, here we have retained the compressible formulation of the Navier-Stokes equation. This is because in many geophysical flows, like in oceans, lava flows, or debris flows, fluids are incompressible but with variable density, for example as a result of spatial and temporal variations in temperature (for instance due to thermal exchanges and cooling of a lava flow), in concentration of sediments (due to settling or erosion processes) or in concentration of salinity.

For some of such flows, when the horizontal length scale is much greater than the vertical length scale and when the vertical dynamics can be neglected compared to horizontal effects

($w = 0$), by integrating over flow thickness it is possible to derive a simpler 2D transient model describing the fluid dynamics. Here, we write this simplified system of equations by adopting an horizontal Cartesian system of coordinates, such that the topography (here assumed not varying with time) is expressed as $B(x, y)$ and the two velocity significant components u and v are defined as the components along the x and y axes respectively, orthogonal to the z axis that is parallel to the gravitational acceleration ($\mathbf{g} = (0, 0, g)$). We introduce now two additional variables describing the system: $h(x, y, t)$, which denotes the fluid thickness above the ground, and $\mathcal{T}(x, y, z, t)$, which denotes the field of an additional transported intensive property, i.e. a local physical property of a system that does not depend on the system size or the amount of material in the system. For simplicity, from now on, we assume that the transported quantity will represent the temperature of the flow, as it would be for a lava flow, and, considering only the temperature advection, we adopt the following transport equation:

$$\frac{\partial \mathcal{T}}{\partial t} + \nabla \cdot (\mathcal{T}\mathbf{u}) = 0. \tag{4}$$

We remark that this equation is general and applicable to other variables, like for examples particle concentration in a sediment-laden flow, where a Rouse profile for the suspension might be used.

Following these assumptions, we introduce the notation $\mathbf{U}(x, y, t)$ for the z-averaged horizontal velocity vector, whose two components U and V are given by

$$U(x, y, t) = \frac{1}{h} \int_B^{B+h} u(x, y, z, t) \, dz, \qquad V(x, y, t) = \frac{1}{h} \int_B^{B+h} v(x, y, z, t) \, dz.$$

Similarly, we introduce the notation T for the depth-averaged temperature

$$T(x, y, t) = \frac{1}{h} \int_B^{B+h} \mathcal{T}(x, y, z, t) \, dz.$$

In a variety of situations density depends on temperature and here we assume a linear dependence of density on the temperature

$$\rho(z) = \rho_0 + m\mathcal{T}.$$

This is the case, for example, of some of the materials (wax and silicone oils) investigated in the examples presented in §3. Furthermore, for the applications we are interested in (for example lava flows or the laboratory analogue experiments simulated in this work), the vertical variations of density are small with respect to the horizontal ones. For this reason, in the following we will consider only horizontal variations of the depth-averaged density, observing that it also depends linearly on the depth-averaged temperature

$$\bar{\rho} := \frac{1}{h} \int_B^{B+h} \rho(z) \, dz = \frac{1}{h} \int_B^{B+h} \left[\rho_0 + m\mathcal{T} \right] dz = mT + \rho_0.$$

For this reason, in the following, we will use for the depth-averaged temperature, without ambiguity, the notation ρ.

1.1. The velocity vertical profile

In the derivation of the classical shallow water model, from the assumption of inviscid fluid it descends that the velocity does not depend on the vertical coordinate, i.e. $\mathbf{u} = \mathbf{u}(x, y, t)$. With this assumption, the depth-averaged velocity $\mathbf{U}$ corresponds to the local velocity. Instead, for a free surface laminar viscous flow, moving in one direction, a vertical velocity profile develops and three conditions must be satisfied: (*i*) null velocity at the bottom, (*ii*) null traction between air and fluid and (*iii*) maximum velocity at the free surface.

As shown in [30], when considering one-directional motion of a Newtonian fully developed laminar viscous flow, the balance of friction and gravitational force leads to a parabolic velocity profile (as represented in Figure 1), similarly to a Poiseuille flow:

$$u(x, z, t) = a(z - B)^2 + b(z - B) + c, \tag{5}$$
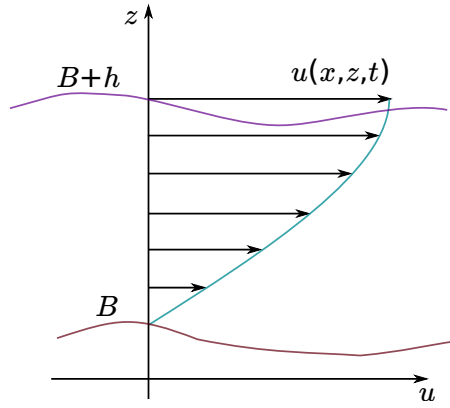
with $a = a(x, t)$, $b = b(x, t)$, $c = c(x, t)$.

Figure 1: Parabolic velocity profile.

By imposing the previous conditions to the form (5) of $u(x, z, t)$, we completely determine its expression:

(*i*) $u(x, B, t) = 0 \iff c(x, t) = 0$, $\forall x$, $\forall t$;

(*ii*) $\partial_z u(x, B + h, t) = 0 \iff b(x, t) = -2 \, h \, a(x, t)$, $\forall x$, $\forall t$;

(*iii*) $u(x, B + h, t) = a(x, t)h^2 + b(x, t)h \iff a(x, t) = -\dfrac{u(x, B + h, t)}{h^2}$, $\forall x$, $\forall t$.

Since for a parabolic profile the relation between maximum and average velocity is $u(x, B + h, t) = \frac{3}{2}U$, by applying (*i*)–(*iii*) we express u in terms of U as

$$u(x, z, t) = \frac{3}{2} U(x, t) \left(1 - \frac{\left(z - B - h(x, t) \right)^2}{h^2(x, t)} \right). \tag{6}$$

In the following, we assume the parabolic profile given by Eq. (6). Then, we finally substitute Eq. (6) into the conservation of mass equation (1) and, integrating over the flow thickness, we obtain:

$$\frac{\partial(\rho h)}{\partial t} + \nabla \cdot (\rho h \mathbf{U}) = 0.$$

When the transient term of the momentum equation (2) is integrated over the flow thickness, because of the assumption that ρ does not depend on the flow depth, we have:

$$\frac{\partial}{\partial t} \int_B^{B+h} \rho \mathbf{u}(\mathbf{x}, z, t) \, dz = \frac{\partial(\rho h \mathbf{U})}{\partial t}.$$

For the derivation of the other terms of the depth-averaged momentum equation, we consider for the sake of simplicity the 1D version of the momentum equation. By substituting the expression for the velocity profile in the advective term and by integrating it, one finds:

$$\int_B^{B+h} \rho \, u^2(x, z, t) \, dz = \beta_u \rho \, h \, U^2, \tag{7}$$

where $\beta_u = \frac{6}{5}$. This coefficient is often termed in literature as *Boussinesq momentum coefficient* or *shape factor*, and its magnitude reflects the shear in the profile of the horizontal fluid velocity. Different velocity profiles, arising for example when non-Newtonian viscosity are considered, will result in different values of β_u. Even though it is frequently set equal to unity (which holds only when velocity is constant over the flow thickness), it is well known that this coefficient may have a significant effect on the dynamics of the flow when a complete sheared flow is expected [11].

1.2. Pressure and viscosity terms

Let assume now a hydrostatic profile for the pressure p, i.e.

$$\frac{\partial p(x, z, t)}{\partial z} = \rho g.$$

Integrating p from the height z to the free surface $B + h$, and fixing at 0 the pressure value at the free surface, we obtain the expression of hydrostatic pressure at height z

$$p(x, z, t) = \int_z^{B+h} \frac{\partial p(x, \zeta, t)}{\partial \zeta} d\zeta = \rho g[(B(x) + h(x, t)) - z]$$

and, deriving with respect to x, we have

$$\frac{\partial p(x, z, t)}{\partial x} = g \frac{\partial}{\partial x}(\rho(B(x) + h(x, t))) - g z \frac{\partial \rho}{\partial x}$$

When this term is integrated with respect to z over the flow thickness, i.e. it is integrated from $z = B$ to $B + h$, we obtain the desired term of the depth-averaged equation accounting

7

for pressure gradient, that is

$$\int_B^{B+h} \frac{\partial p\,(x,z,t)}{\partial x}\,dz = gh\frac{\partial}{\partial x}\left[\rho\,(B+h)\right] - g\frac{\partial \rho}{\partial x}\left[\frac{z^2}{2}\right]_B^{B+h} =$$
$$\rho gh\left(\frac{\partial h}{\partial x} + \frac{\partial B}{\partial x}\right) + \frac{1}{2}gh^2\frac{\partial \rho}{\partial x}.$$

By rearranging the derivatives, the depth-integrated pressure gradient reduces to

$$\int_B^{B+h} \frac{\partial p}{\partial x}\,dz = \frac{\partial}{\partial x}\left(\frac{1}{2}\rho gh^2\right) + \rho gh\frac{\partial B}{\partial x}, \tag{8}$$

which is the term usually found in depth-averaged momentum equations in presence of a variable topography.

Finally, we obtain the expression for the viscous term of the depth-averaged equation by integrating vertically the term $\nabla \cdot \left[\mu(\nabla \mathbf{u} + (\nabla \mathbf{u})^T)\right]$ appearing in the Navier-Stokes equations (where μ is the dynamic viscosity, according to (2) and (3)), which here reduces to $\mu \Delta \mathbf{u}$ because the fluid is incompressible. By considering again a one-directional motion, the integral results in

$$\int_B^{B+h} \mu\frac{\partial^2 u}{\partial z^2}\,dz = \mu\left.\frac{\partial u}{\partial z}\right|_B^{B+h} = \mu\left[\frac{\partial u}{\partial z}(x,B+h,t) - \frac{\partial u}{\partial z}(x,B,t)\right] \overset{(*)}{=} -\mu\,\partial_z u(x,B,t), \tag{9}$$

where in $(*)$ we have considered again no traction between air and fluid, as done for the parabolic velocity profile assumption. In particular, according with the parabolic profile expressed in Eq. (6), the vertical derivative evaluated at the bottom is

$$\partial_z u(x,B,t) = 3\frac{U(x,t)}{h}$$

so that the viscous term expression becomes

$$\int_B^{B+h} \mu\frac{\partial^2 u}{\partial z^2}\,dz = -\rho\gamma U(x,t),$$

where $\gamma := \dfrac{3\nu}{h}$ is the friction coefficient, depending on kinematic viscosity and flow thickness (by reminding the relationship between dynamic and kinematic viscosity: $\mu = \rho\nu$). Note that Gerbeau and Perthame [31], by using a different approach, obtained a similar expression for γ.

1.3. The temperature vertical profile

As previously stated, we do not assume that temperature is constant over the whole flow depth. We assume instead that temperature variations occur only over a fraction of the flow thickness near the ground, and we denote this region as *characteristic thermal boundary*
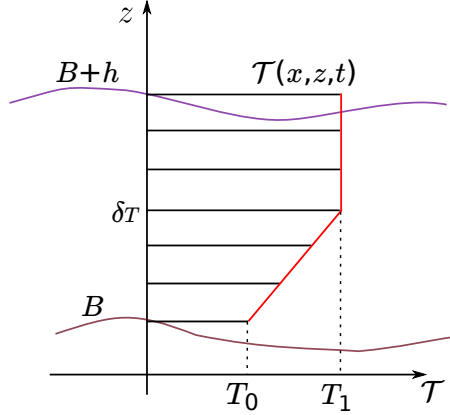
Figure 2: Vertical temperature profile.

layer, with thickness $\delta_T = h/n$ (with $n \geq 1$). We also assume a linear temperature profile near the ground and a constant temperature for $z > \delta_T$, fixing the free-surface temperature at $\mathcal{T} = T_1$ (see Figure 2).

Temperature $\mathcal{T}(x, z, t)$ along a vertical profile can be written in terms of the averaged temperature T, of the free-surface temperature T_1 and of the thickness index n as follows:

$$
\mathcal{T}(x, z, t) = \begin{cases} \dfrac{2n^2}{h}\big(T_1 - T(x, t)\big)z + (1 - 2n)T_1 + 2nT(x, t), & \text{if} \quad 0 \leq z \leq \delta_T \\[2ex] T_1, & \text{if} \quad \delta_T < z \leq h. \end{cases}
$$

When we use this expression for the piecewise linear temperature profile and Eq. (6) for the parabolic velocity profile, the integration over the vertical depth of the advective term appearing in Eq. (4) leads to the sum of two terms whose coefficients depend on the parameter n related to the thermal boundary layer thickness h/n

$$
\int_B^{B+h} \mathcal{T}(x, z, t)\, u(x, z, t)\, dz = \frac{4n^2 - n}{4n^3}hTU + \frac{4n^3 - 4n^2 + n}{4n^3}hT_1U.
$$

Now, if we denote by β_T the coefficient of the first term on the right-hand side of the previous equation and by β_{T_1} the coefficient of the second term, we obtain the 1D formulation of the advective flux

$$
(\beta_T T + \beta_{T_1} T_1)\, hU.
$$

Being $0 \leq \beta_T, \beta_{T_1} \leq 1$ and $\beta_T + \beta_{T_1} = 1$, the term in brackets in the previous equation corresponds to a convex combination of the maximum and averaged temperature. For instance, when considering $n = 4$ (as suggested by Costa and Macedonio [2] for lava model), the values of the two coefficients are $\beta_T \approx 0.24$ and $\beta_{T_1} \approx 0.76$. One observes that the smaller is the thickness of the thermal boundary layer, the closer to 1 is the value of β_{T_1} and the smaller is the value of β_T. Thus, when the boundary layer thickness goes to zero (n goes to $+\infty$) the maximum temperature and the depth-averaged temperature coincide and

9

the advective term in (4) reduces to

$$\nabla \cdot \big(Th\mathbf{U} \big), \tag{10}$$

which is the classical form resulting from the assumption of a uniform temperature profile (hence $T = T_1$) and corresponds to the choices $\beta_{T_1} = 1$ and $\beta_T = 0$.

In summary, assuming an incompressible homogeneous fluid, a hydrostatic pressure distribution, a parabolic velocity profile, a piecewise linear temperature profile and generalizing to the two-dimensional case, the depth-averaged equations for the flow are:

$$\frac{\partial(\rho h)}{\partial t} + \nabla \cdot (\rho h \mathbf{U}) = 0, \tag{11}$$

$$\frac{\partial(\rho h \mathbf{U})}{\partial t} + \nabla \cdot \big(\beta_u \rho h \mathbf{U} \mathbf{U}^T \big) + \nabla \left(\frac{1}{2} \rho g h^2 \right) = -\rho g h \nabla B - \rho \gamma \mathbf{U}, \tag{12}$$

$$\frac{\partial(hT)}{\partial t} + \nabla \cdot \big(h(\beta_T\, T + \beta_{T_1}\, T_1)\mathbf{U} \big) = 0, \tag{13}$$

where we underline that $\mathbf{U}$ is a column vector; the system is coupled with the state equation that considers the density dependence on the average temperature

$$\rho(T) = mT + \rho_0. \tag{14}$$

The stationary steady-state solutions of our system are the *lake-at-rest* conditions:

$$\mathbf{U} = 0, \quad B + h = \text{const}, \quad T = \text{const}, \quad \rho = \text{const}, \tag{15}$$

The homogeneous part of the system (11–13) is constituted by non-linear hyperbolic PDEs, and thus it is solved by classical numerical techniques developed for such kind of equations [32, 33]. In order to do that, we first rewrite the homogeneous system in a more compact notation, introducing the vector of *conservative variables* $\mathbf{q}$

$$\mathbf{q} = \begin{bmatrix} q_1 \\ q_2 \\ q_3 \\ q_4 \end{bmatrix} := \begin{bmatrix} \rho h \\ \rho h U \\ \rho h V \\ hT \end{bmatrix}.$$

If we denote by $\mathbf{f} = (\mathbf{G}, \mathbf{H})$ the flux vector (argument of the divergence in (11–13)), and we express the fluxes as function of the conservative variables

$$\mathbf{G}(\mathbf{q}) = \begin{bmatrix} \rho h U \\ \beta_u \rho h U^2 + \dfrac{\rho g}{2} h^2 \\ \beta_u \rho h U V \\ h\big(\beta_T T + \beta_{T_1} T_1\big)U \end{bmatrix}, \quad \mathbf{H}(\mathbf{q}) = \begin{bmatrix} \rho h V \\ \beta_u \rho h U V \\ \beta_u \rho h V^2 + \dfrac{\rho g}{2} h^2 \\ h\big(\beta_T T + \beta_{T_1} T_1\big)V \end{bmatrix},$$

then we rewrite the homogeneous part of the governing equations as

$$\frac{\partial \mathbf{q}}{\partial t} + \nabla \cdot (\mathbf{f}(\mathbf{q})) \equiv \frac{\partial \mathbf{q}}{\partial t} + \frac{\partial \mathbf{G}(\mathbf{q})}{\partial x} + \frac{\partial \mathbf{H}(\mathbf{q})}{\partial y}. \tag{16}$$

In order to study the hyperbolicity and local propagation velocities, we replace the homogeneous system by the equivalent quasi-linear formulation

$$\mathbf{q}_t + \nabla \cdot (\mathbf{f}(\mathbf{q})) = 0 \quad \longleftrightarrow \quad \mathbf{q}_t + \mathbf{G}'(\mathbf{q})\mathbf{q}_x + \mathbf{H}'(\mathbf{q})\mathbf{q}_y = 0,$$

where $\mathbf{G}'$ and $\mathbf{H}'$ are the Jacobian matrices of the advective fluxes. By direct computation, it is possible to show that each of the two Jacobians has four eigenvalues, which are the elements of the following spectra:

$$\begin{aligned} Sp\,(\mathbf{G}') &= \left\{ \beta_u\, U \pm \sqrt{\beta_u(\beta_u - 1)U^2 + gh},\ \beta_u\, U,\ \beta_T U \right\}, \\ Sp\,(\mathbf{H}') &= \left\{ \beta_u\, V \pm \sqrt{\beta_u(\beta_u - 1)V^2 + gh},\ \beta_u\, V,\ \beta_T V \right\}. \end{aligned} \tag{17}$$

When the eigenvalues are real, it follows that the equations are hyperbolic, and the perturbations in the solution propagate with finite velocities given by the previous equations. We also note that, when $\beta_u = 1$ (resulting from the assumption of a uniform velocity profile), the first eigenvalues reduce to

$$U \pm \sqrt{gh} \quad \text{and} \quad V \pm \sqrt{gh},$$

thus they coincide with the characteristic velocities of the classical shallow water equations.

Recall that the Froude number is a dimensionless variable accounting for the relative importance of inertial and gravitational forces. Classically, the Froude number for shallow water waves is defined as

$$Fr = \frac{|\mathbf{U}|}{\sqrt{gh}}, \tag{18}$$

see Leveque 2004 [32], and according to the value assumed by this ratio, the regime is classified as subcritical if $Fr < 1$, critical if $Fr = 1$ and supercritical if $Fr > 1$. When flow conditions are supercritical, surface waves generated by downstream disturbances cannot travel upstream. Conversely, when flow is subcritical, disturbance propagates both upstream and downstream. This classification is relevant also for numerical simulations, because the boundary conditions must be prescribed according to the flow regime. We point out that the effects of a parabolic velocity profile assumption on the solution become less important as the Froude number approaches 0, because in such situations the dynamics are less affected by the inertial term.

As shown above, the parabolic velocity profile defined in Eq. (6) leads to the presence of the coefficient β_u in the inertial term appearing in the momentum equation. Because of that, from a mathematical point of view, also the critical conditions change with respect to the classical shallow water equations. In fact, considering the 1D case, the eigenvalues

11

of the flux Jacobian for the parabolic velocity case have the same sign when the following condition is satisfied:
$$\frac{|U|}{\sqrt{(1 - 1/\beta_u)U^2 + gh/\beta_u^2}} > 1.$$

According to this formulation, for the same value of the flow thickness h, the critical regime for a parabolic profile is obtained at a smaller depth-averaged flow velocity than for constant velocity profile. In addition, we observe that the left-hand side quantity converges to the Froude number when the velocity tends to have constant profile, namely when β_u goes to 1.

2. Numerical model

The numerical model we have developed leans on the central-upwind second order scheme introduced by A. Kurganov and G. Petrova in 2007 [17], as far as the spatial derivative concerns, and on an Implicit-Explicit scheme belonging to the Runge-Kutta family described by Pareschi and Russo in 2000 [34] for the discretization in time.

2.1. Spatial discretization

Kurganov and Petrova [17] (KP in the following) developed a numerical scheme to solve the classical shallow water equations which, on one hand, is able to capture stationary steady-states solutions (like lake at rest), on the other, guarantees the positivity preserving property of fluid thickness.

For simplicity, we present the numerical scheme for the one dimensional version of the system (11-13) (for the discretization of the two dimensional version, consult de' Michieli Vitturi et al. [27]):

$$\begin{cases} (\rho h)_t + (\rho h U)_x = 0, \\ (\rho h U)_t + \left(\beta_u \rho h U^2 + \frac{\rho g}{2}h^2 \right)_x = -\rho g h B_x - \rho \gamma U, \\ \left(h T \right)_t + \left(h \big(\beta_T T + \beta_{T_1} T_1 \big) U \right)_x = 0, \end{cases} \tag{19}$$

coupled with the state equation for the temperature dependent density $\rho = mT + \rho_0$. Naming $\mathbf{q}$ the vector of conservative variables, we denote by $\mathbf{f}(\mathbf{q})$ the vector of the fluxes and the source terms by $\mathbf{E}(\mathbf{q})$ and $\mathbf{S}(\mathbf{q})$:

$$\mathbf{q} = \begin{bmatrix} \rho h \\ \rho h U \\ h T \end{bmatrix}, \quad \mathbf{f}(\mathbf{q}) = \begin{bmatrix} \rho h U \\ \beta_u \rho h U^2 + \frac{\rho g}{2}h^2 \\ h \big(\beta_T T + \beta_{T_1} T_1 \big) U \end{bmatrix}, \quad \mathbf{E}(\mathbf{q}) = \begin{bmatrix} 0 \\ -\rho g h B_x \\ 0 \end{bmatrix}, \quad \mathbf{S}(\mathbf{q}) = \begin{bmatrix} 0 \\ -\rho \gamma U \\ 0 \end{bmatrix},$$

so that we can write the 1D system in the compact form:

$$\frac{\partial \mathbf{q}}{\partial t} + \frac{\partial \mathbf{f}(\mathbf{q})}{\partial x} = \mathbf{E}(\mathbf{q}) + \mathbf{S}(\mathbf{q}). \tag{20}$$

12

The distinction between the two source terms will be exploited in §2.2.

In order to apply a Finite Volume scheme, the domain is divided into a uniform grid, and for each cell we denote by x_i its midpoint and indicate by $C_i = \left[x_{i-\frac{1}{2}}, x_{i+\frac{1}{2}}\right]$ the i-th cell. An important feature of a numerical scheme discretizing the system of Eqs. (19) is a proper treatment of the topography. Here, as a preliminary step, the original topography $B(x)$ is approximated by a continuous linear-piecewise function $\tilde{B}(x)$, whose values $\tilde{B}_{i+\frac{1}{2}}$ at the interfaces $x_{i+\frac{1}{2}}$ are obtained by averaging the limits of $B(x)$ from both the sides. The approximation $\tilde{B}$ and its derivative are used for the finite-volume numerical discretization in the cell C_i of the second component of the source term $\mathbf{E}(\mathbf{q})$:

$$\frac{1}{\Delta x} \int_{x_{i-\frac{1}{2}}}^{x_{i+\frac{1}{2}}} (-\rho g h B_x) dx \approx -g \rho_i h_i \frac{\tilde{B}_{i+\frac{1}{2}} - \tilde{B}_{i-\frac{1}{2}}}{\Delta x}. \tag{21}$$

We denote by $\mathbf{Q}_i$ the approximation of the average of $\mathbf{q}(\cdot, t)$ over the i-th cell

$$\mathbf{Q}_i(t) \approx \frac{1}{\Delta x} \int_{x_{i-\frac{1}{2}}}^{x_{i+\frac{1}{2}}} \mathbf{q}(x, t) dx \ ,$$

then we apply a semi-discretization of Eqs. (20) obtaining the following system of ODEs in each cell:

$$\frac{d}{dt} \mathbf{Q}_i(t) = -\frac{\mathbf{F}_{i+\frac{1}{2}}(t) - \mathbf{F}_{i-\frac{1}{2}}(t)}{\Delta x} + \mathbf{E}_i(t) + \mathbf{S}_i(t) \tag{22}$$

where $\mathbf{F}_{i\pm\frac{1}{2}}$ are the numerical fluxes, here defined accordingly with KP. Our modified version of the central-upwind finite volume KP scheme is briefly summarized in the following steps (see the original reference [17] for details).

(1) Solution reconstruction. From the values of the conservative variables $\mathbf{Q}$, we compute an additional set of variables $\mathbf{P} = [w, U, T]^T$ (where $w := h + B$ denotes the free-surface height), by using the following relations

$$h = \frac{\mathbf{Q}^{(1)} - m\mathbf{Q}^{(3)}}{\rho_0}, \quad T = \frac{\mathbf{Q}^{(3)}}{h}, \quad \rho = mT + \rho_0, \quad U = \frac{\mathbf{Q}^{(2)}}{\rho h}.$$

When the height h is very small, an appropriate de-singularization procedure is necessary, in order to prevent inaccuracies in velocity and temperature values. To do that, we adopt the following expressions to compute the temperature and velocity values instead of the previous ones

$$T = \frac{\sqrt{2} h \mathbf{Q}^{(3)}}{\sqrt{h^4 + \max(h^4, \varepsilon)}}, \quad U = \frac{\sqrt{2} h \mathbf{Q}^{(2)}}{\rho \sqrt{h^4 + \max(h^4, \varepsilon)}}$$

as suggested in [17].

By using the cell values $\{\mathbf{P}_i\}_i$ calculated from the cell averages $\{\mathbf{Q}_i\}_i$, we define a discontinuous piecewise linear reconstruction over each cell:

$$\tilde{\mathbf{p}}_i(x) = \mathbf{P}_i + \boldsymbol{\sigma}_i(x - x_i), \quad x_{i-\frac{1}{2}} < x < x_{i+\frac{1}{2}}, \quad \forall i, \tag{23}$$

13

where the slopes $\{\boldsymbol{\sigma}_i\}_i$ are computed by using a suitable geometric limiter. The reconstructed solution might be discontinuous at the interfaces points $x_{i+\frac{1}{2}}$, then we define $\mathbf{P}^L_{i+\frac{1}{2}}$ and $\mathbf{P}^R_{i+\frac{1}{2}}$ as the left and right side values of the reconstructed solution respectively.

In addition, a suitable correction is needed for the reconstructed values $w^{L/R}_{i+\frac{1}{2}}m$, in order to preserve the positivity of each $h^{L/R}_{i+\frac{1}{2}} := w^{L/R}_{i+\frac{1}{2}} - \tilde{B}_{i+\frac{1}{2}}$ (not guaranteed by the geometric limiters) as described in [17].

The solution reconstruction is a key point to guarantee the well-balancing property of a numerical scheme. In §2.1.1, we show that the modification introduced here with respect to [17] continues to guarantee this property, even if the equations are modified and the linear reconstruction is computed for a different set of variables.

(2) Values of the conservative variables at the interfaces. From the values $\mathbf{P}^L_{i+\frac{1}{2}}$ and $\mathbf{P}^R_{i+\frac{1}{2}}$ of the variables at the interfaces, we compute $\mathbf{Q}^L_{i+\frac{1}{2}}$ and $\mathbf{Q}^R_{i+\frac{1}{2}}$, namely the values of the conservative variables at the interfaces.

(3) Estimation of the local speed through the interfaces. The reconstructed solution propagates with right-sided and left-sided local speeds $a^{\pm}_{i+\frac{1}{2}}$, which are estimated in terms of the eigenvalues of the Jacobian of $\mathbf{f}$, denoted by $\mathbf{f}'$, as we have seen in (17) for 2D model, at the reconstructed values $\mathbf{Q}^{R/L}_{i+\frac{1}{2}}$:

$$
\begin{aligned}
a^+_{i+1/2} &= \max\left\{\lambda_{\max}\left(\mathbf{f}'\left(\mathbf{Q}^R_{i+\frac{1}{2}}\right)\right), \lambda_{\max}\left(\mathbf{f}'\left(\mathbf{Q}^L_{i+\frac{1}{2}}\right)\right), 0\right\}, \\
a^-_{i+1/2} &= \min\left\{\lambda_{\min}\left(\mathbf{f}'\left(\mathbf{Q}^R_{i+\frac{1}{2}}\right)\right), \lambda_{\min}\left(\mathbf{f}'\left(\mathbf{Q}^L_{i+\frac{1}{2}}\right)\right), 0\right\}.
\end{aligned}
\tag{24}
$$

The computation of U is requested also here, but in this occasion the de-singularization is not necessary: we did it previously passing to the set of variables $\mathbf{P}$, with those values we have done the linear reconstruction, and since we have used geometric limiters, then all the velocities are limited at the interfaces.

(4) Computation of the numerical flux. We adopt the numerical flux expression used in [17], that is:

$$
\mathbf{F}_{i+\frac{1}{2}}(t) = \frac{a^+_{i+\frac{1}{2}}\mathbf{f}\left(\mathbf{Q}^L_{i+\frac{1}{2}}\right) - a^-_{i+\frac{1}{2}}\mathbf{f}\left(\mathbf{Q}^R_{i+\frac{1}{2}}\right)}{a^+_{i+\frac{1}{2}} - a^-_{i+\frac{1}{2}}} + \frac{a^+_{i+\frac{1}{2}} a^-_{i+\frac{1}{2}}}{a^+_{i+\frac{1}{2}} - a^-_{i+\frac{1}{2}}}\left[\mathbf{Q}^R_{i+\frac{1}{2}} - \mathbf{Q}^L_{i+\frac{1}{2}}\right]
\tag{25}
$$

where the first term on the right side is an average of the evaluated fluxes weighted with the speeds of propagation, because the total flux at the interface depends both on the left-going and on the right-going fluxes, each weighted with the maximum speed in that direction. Notice that the time dependence of the right term, although it is omitted explicitly, belongs to both $a^{\pm}_{i+\frac{1}{2}}$ and $\mathbf{Q}^{R/L}_{i+\frac{1}{2}}$.

With respect to [17], the model equations we refer to are richer, since we have an additional equation for the temperature transport, corrector coefficients β_u, β_T and β_{T_1} inside the flux terms, more source terms and also a variable density. From the numerical point of view, a major difference between our scheme and the original KP scheme is that we pass forward and backward to the set of variables $\mathbf{P}$ to compute the solution reconstruction of the conservative variables at the interfaces. Moreover, the presence of the corrector coefficients β_u and β_T impacts over the scheme by affecting the local speed of propagation.

2.1.1. Well-balancing property

As stated before, the modifications introduced here to the numerical scheme presented in [17] continue to guarantee the well-balancing property for stationary steady states. We provide a sketch of proof of this property.

One recalls that the stationary steady-state solutions of our system consist of null velocity and constant conditions for both free surface height, temperature and density (see equations (15)). In such cases, from the system of equations (20) we obtain:

$$\partial_x \left(\frac{1}{2} \rho g h^2 \right) = -\rho g h B_x. \tag{26}$$

By proving that the equality (26) is preserved also by the numerical discretization, we confirm the well-balancing of the numerical scheme.

The flux term on the left side is discretized with the numerical fluxes $\mathbf{F}^{(2)}_{i-\frac{1}{2}}$ and $\mathbf{F}^{(2)}_{i+\frac{1}{2}}$ defined in Eq. (25). Since velocity is null, the conservative variable $\mathbf{Q}^{(2)} = \rho h U$ is null too, therefore the numerical flux at the right interface of the cell i reduces to:

$$\mathbf{F}^{(2)}_{i+\frac{1}{2}} = \frac{a^+_{i+\frac{1}{2}} \mathbf{f}^{(2)}\left(\mathbf{Q}^L_{i+\frac{1}{2}}\right) - a^-_{i+\frac{1}{2}} \mathbf{f}^{(2)}\left(\mathbf{Q}^R_{i+\frac{1}{2}}\right)}{a^+_{i+\frac{1}{2}} - a^-_{i+\frac{1}{2}}}, \tag{27}$$

where the flux values at the sides of the interfaces are given by $\mathbf{f}^{(2)}\left(\mathbf{Q}^{L/R}_{i+\frac{1}{2}}\right) = \frac{1}{2} \rho^{L/R}_{i+\frac{1}{2}} g \left(h^{L/R}_{i+\frac{1}{2}}\right)^2$. According to the numerical scheme, the linear reconstruction is applied to the free surface $w = h + B$ to find its interface values $w^L_{i+\frac{1}{2}}$ and $w^R_{i+\frac{1}{2}}$, from which we derive the interface values of h as

$$h^L_{i+\frac{1}{2}} = w^L_{i+\frac{1}{2}} - \tilde{B}_{i+\frac{1}{2}}, \quad h^R_{i+\frac{1}{2}} = w^R_{i+\frac{1}{2}} - \tilde{B}_{i+\frac{1}{2}}.$$

As the total thickness $w = h + B$ is constant, its reconstructed values on the left and right sides of each interface are equal, hence the same condition descends for h:

$$w^L_{i+\frac{1}{2}} = w^R_{i+\frac{1}{2}} \Rightarrow h^L_{i+\frac{1}{2}} = h^R_{i+\frac{1}{2}}.$$

From the assumption of constant density, we also have $\rho^L_{i+\frac{1}{2}} = \rho^R_{i+\frac{1}{2}} = \rho$ and from now we neglect the L/R notation for the interface values of h and ρ. According with these considerations, the numerical flux simplifies its expression

$$\mathbf{F}^{(2)}_{i+\frac{1}{2}} = \frac{a^+_{i+\frac{1}{2}} \left[\frac{1}{2} \rho g \left(h_{i+\frac{1}{2}}\right)^2\right] - a^-_{i+\frac{1}{2}} \left[\frac{1}{2} \rho g \left(h_{i+\frac{1}{2}}\right)^2\right]}{a^+_{i+\frac{1}{2}} - a^-_{i+\frac{1}{2}}} = \frac{1}{2} \rho g \left(h_{i+\frac{1}{2}}\right)^2$$

and the complete discretization of the flux term on the LHS of the stationary state Eq. (26) becomes

$$\frac{\mathbf{F}^{(2)}_{i+\frac{1}{2}} - \mathbf{F}^{(2)}_{i-\frac{1}{2}}}{\Delta x} = \frac{1}{2\Delta x}\rho g\left[\left(h_{i+\frac{1}{2}}\right)^2 - \left(h_{i-\frac{1}{2}}\right)^2\right] = \rho g h_i \frac{h_{i+\frac{1}{2}} - h_{i-\frac{1}{2}}}{\Delta x}, \qquad (28)$$

where, because of the linearity of the interface reconstruction, h_i is the average of the interface values.

We observe that the discretization of the right term of Eq. (26), given by Eq. (21), can be written in the following equivalent way

$$-g\rho_i h_i \frac{\tilde{B}_{i+\frac{1}{2}} - \tilde{B}_{i-\frac{1}{2}}}{\Delta x} = -g\rho h_i \frac{\left(w_{i+\frac{1}{2}} - h_{i+\frac{1}{2}}\right) - \left(w_{i-\frac{1}{2}} - h_{i-\frac{1}{2}}\right)}{\Delta x}. \qquad (29)$$

Because of the constant condition on the free surface, we have that $w_{i-\frac{1}{2}} = w_{i+\frac{1}{2}}$ and, by canceling these terms in the previous equation, we find the same expression as in Eq. (28), so we conclude the proof.

2.1.2. Positivity-preserving property

In [17] has been proven that, for their model, an explicit temporal discretization of the central-upwind scheme with an appropriate choice of the time step, is not only well-balanced, but also positivity preserving for h. Despite the differences from them, for our modified scheme their result is still valid, but with an additional condition over the β's.

We premise in a specific lemma the nontrivial adjustments to the proof of the corresponding result in [17].

Lemma 1. *If the condition* $\max(\beta_u, \beta_T) \geq 1$ *is verified, then for each interface the following inequalities hold:*

$$(a) \quad a^-_{i+\frac{1}{2}} \leq U^R_{i+\frac{1}{2}}, \quad (b) \quad a^-_{i+\frac{1}{2}} \leq U^L_{i+\frac{1}{2}}, \quad (c) \quad a^+_{i+\frac{1}{2}} \geq U^R_{i+\frac{1}{2}}, \quad (d) \quad a^+_{i+\frac{1}{2}} \geq U^L_{i+\frac{1}{2}}.$$

PROOF. *(a)* We start by distinguishing the different cases of positive or negative velocities. In the first case $0 \leq U^R_{i+\frac{1}{2}}$, and by definition $a^-_{i+\frac{1}{2}} \leq 0$, therefore the thesis follows. Instead when $U^R_{i+\frac{1}{2}} < 0$ it is sufficient to show that $\lambda_{\min}\left(\mathbf{f}'\left(\mathbf{Q}^R_{i+\frac{1}{2}}\right)\right) \leq U^R_{i+\frac{1}{2}}$.

A simple check shows that, for any $\mathbf{q}$, the matrix $\mathbf{f}'(\mathbf{q})$ is block lower triangular; if $\mathbf{f}'_u(\mathbf{q})$ denotes its leading (full) 2×2 principal submatrix, then the relations

$$\lambda_{\min}\left(\mathbf{f}'(\mathbf{q})\right) = \min\left\{\lambda_{\min}\left(\mathbf{f}'_u(\mathbf{q})\right), \beta_T U\right\}, \quad \lambda_{\max}\left(\mathbf{f}'(\mathbf{q})\right) = \max\left\{\lambda_{\max}\left(\mathbf{f}'_u(\mathbf{q})\right), \beta_T U\right\}$$

hold.

Now we suppose by contradiction that $\lambda_{\min}\left(\mathbf{f}'\left(\mathbf{Q}^R_{i+\frac{1}{2}}\right)\right) > U^R_{i+\frac{1}{2}}$, so that on one hand $\beta_T U^R_{i+\frac{1}{2}} > U^R_{i+\frac{1}{2}}$ which implies $\beta_T < 1$ because the velocity is assumed negative. On the other

hand, at the same time we must have $\lambda_{\min}\left(\mathbf{f}'_u\left(\mathbf{Q}^R_{i+\frac{1}{2}}\right)\right) > U^R_{i+\frac{1}{2}}$ so that every eigenvalue of $\mathbf{f}'_u$ is greater than the velocity; this would imply

$$tr\left(\mathbf{f}'_u\left(\mathbf{Q}^R_{i+\frac{1}{2}}\right)\right) > 2\,U^R_{i+\frac{1}{2}},$$

where $tr(\cdot)$ denotes the trace of a matrix which equals the sum of its eigenvalues. A direct computation of the diagonal entries in the Jacobian shows that

$$tr\left(\mathbf{f}'_u\left(\mathbf{Q}^R_{i+\frac{1}{2}}\right)\right) = 2\beta_u U^R_{i+\frac{1}{2}}, \tag{30}$$

but since we are considering a negative velocity this is equivalent to $\beta_u < 1$, which conflicts with the lemma hypothesis since we have proved that $\beta_T < 1$.

(b) The proof is the same as the previous one, with the difference that $\lambda_{\min}\left(\mathbf{f}'\left(\mathbf{Q}^L_{i+\frac{1}{2}}\right)\right)$ must be compared with $U^L_{i+\frac{1}{2}}$.

(c) Again we distinguish the cases of positive and negative velocity. In the case where $U^R_{i+\frac{1}{2}} \leq 0$, the thesis immediately follows by the definition of the propagation speed, for which $a^+_{i+\frac{1}{2}} \geq 0$. Instead if $U^R_{i+\frac{1}{2}} > 0$, we apply the same argument as in (a): suppose by contradiction that $\lambda_{\max}\left(\mathbf{f}'\left(\mathbf{Q}^R_{i+\frac{1}{2}}\right)\right) < U^R_{i+\frac{1}{2}}$ so that both the conditions $\beta_T U^R_{i+\frac{1}{2}} < U^R_{i+\frac{1}{2}}$ (from which $\beta_T < 1$ follows) and $\lambda_{\max}\left(\mathbf{f}'_u\left(\mathbf{Q}^R_{i+\frac{1}{2}}\right)\right) < U^R_{i+\frac{1}{2}}$ hold. On one hand,

$$tr\left(\mathbf{f}'_u\left(\mathbf{Q}^R_{i+\frac{1}{2}}\right)\right) < 2\,U^R_{i+\frac{1}{2}};$$

on the other hand, from (30) the positive sign of velocity yields $\beta_u < 1$, which contradicts the condition on the β coefficients.

(d) The proof is the same as the previous one, with the difference that we must compare $\lambda_{\max}\left(\mathbf{f}'\left(\mathbf{Q}^L_{i+\frac{1}{2}}\right)\right)$ with $U^L_{i+\frac{1}{2}}$.

Theorem 2. *Consider the system of ODEs (22) and the central-upwind semi-discrete scheme described above. Assume that the system is solved by the forward Euler method, which produces a time sequence $\{\mathbf{Q}^n_i\}_i$ of approximations (from which the current value of the height h^n_i is retrieved). Suppose that, for all i, $h^n_i \geq 0$. Then, for all i, $h^{n+1}_i \geq 0$, provided that*

(i) $\max(\beta_u, \beta_T) \geq 1$,

(ii) $\Delta t \leq \dfrac{\Delta x}{2a}$, *where* $a := \max_i\left\{\max\left\{a^+_{i+\frac{1}{2}}, -a^-_{i+\frac{1}{2}}\right\}\right\}$ *and* $a^\pm_{i+\frac{1}{2}}$ *are the local speeds estimated at step 3.*

PROOF. We report only a brief sketch of the proof because it is mainly similar to that presented in Kurganov and Petrova [17], where further details are offered.

Since we are interested in the behaviour of h_i^{n+1}, we focus on the first equation of the system discretized by the forward Euler method; then we rearrange the expression by using the definition (25) of the numerical flux at the interfaces and by considering the value of h_i^n as the average of the reconstructed values at the interfaces. We obtain the following expression for h_i^{n+1}, where $\lambda = \Delta t / \Delta x$

$$h_i^{n+1} = h_{i-\frac{1}{2}}^R \left[\frac{1}{2} + \left(\lambda a_{i-\frac{1}{2}}^- \right) \left(\frac{a_{i-\frac{1}{2}}^+ - U_{i-\frac{1}{2}}^R}{a_{i-\frac{1}{2}}^+ - a_{i-\frac{1}{2}}^-} \right) \right] + h_{i+\frac{1}{2}}^L \left[\frac{1}{2} - \left(\lambda a_{i+\frac{1}{2}}^+ \right) \left(\frac{U_{i+\frac{1}{2}}^L - a_{i+\frac{1}{2}}^-}{a_{i+\frac{1}{2}}^+ - a_{i+\frac{1}{2}}^-} \right) \right]$$
$$+ h_{i-\frac{1}{2}}^L \left(\lambda a_{i-\frac{1}{2}}^+ \right) \left(\frac{U_{i-\frac{1}{2}}^L - a_{i-\frac{1}{2}}^-}{a_{i-\frac{1}{2}}^+ - a_{i-\frac{1}{2}}^-} \right) + h_{i+\frac{1}{2}}^R \left(-\lambda a_{i+\frac{1}{2}}^- \right) \left(\frac{a_{i+\frac{1}{2}}^+ - U_{i+\frac{1}{2}}^R}{a_{i+\frac{1}{2}}^+ - a_{i+\frac{1}{2}}^-} \right) \tag{31}$$

where all the RHS terms are considered at time t_n, but, in order to simplify the notation, we have omitted the superscripts n. Thus h_i^{n+1} is a linear combination of the previous values at the interfaces $h_{i\pm\frac{1}{2}}^{R/L}$ with suitable coefficients. The special reconstruction procedure at the interfaces guarantees that all $h_{i\pm\frac{1}{2}}^{R/L} \geq 0$. From the definition of the propagation speeds (24) it follows that $a_{i-\frac{1}{2}}^+ \geq 0$, $a_{i+\frac{1}{2}}^- \leq 0$, $a_{i\pm\frac{1}{2}}^+ - a_{i\pm\frac{1}{2}}^- \geq 0$. Thanks to assumption (i), we apply Lemma 1 which implies

$$0 \leq \frac{a_{i\pm\frac{1}{2}}^+ - U_{i\pm\frac{1}{2}}^R}{a_{i\pm\frac{1}{2}}^+ - a_{i\pm\frac{1}{2}}^-} \leq 1 \quad \text{and} \quad 0 \leq \frac{U_{i\pm\frac{1}{2}}^L - a_{i\pm\frac{1}{2}}^-}{a_{i\pm\frac{1}{2}}^+ - a_{i\pm\frac{1}{2}}^-} \leq 1.$$

By adding the further CFL condition $\lambda a \leq 1/2$ ensured by assumption (ii), we conclude that all the coefficients in (31) are non-negative, therefore the fluid depth computed at the next time level h_i^{n+1} is a sum of non-negative terms for all i, and the proof is completed.

Remark 1. In the 2D case, assumption (ii) becomes $\Delta t \leq \min \left\{ \dfrac{\Delta x}{4a}, \dfrac{\Delta y}{4b} \right\}$, where $\Delta x, \Delta y$ are the spatial steps along the two horizontal directions whereas a, b are the maximum local speeds of propagation at interfaces along the x- and y-axis respectively. Assumption (i) does not change and the proof of the analogous of Lemma 1 is essentially the same: the Jacobians are 4×4 matrices but keep a block triangular structure (up to permutation as $\mathbf{H}'(\mathbf{q})$ is concerned), according to the spectra displayed in (17).

Moreover, our derivation of β_u from a velocity profile never leads to a value less than 1, so that assumption (i) is always true. In fact, for any arbitrary profile $u(x, z, t)$ the equality

$$\int_B^{B+h} u^2(x, z, t) \, dz = \beta_u \, h \, U^2$$

must be imposed, as we have seen in (7) for the parabolic profile. If we consider for each (x, t) the L^2 space over the set $\{z : B \leq z \leq B + h\}$, the left side of the equation sees the squared L^2 norm of u; by Schwarz inequality,

$$\|u\|_{L^2}^2 \geq \frac{|\langle u, 1 \rangle_{L^2}|^2}{\|1\|_{L^2}^2}$$

18

where the inner product in the numerator corresponds to $\int_B^{B+h} u(x, z, t)dz = h\, U(x, t)$ whereas the denominator equals h. Therefore $\beta_u\, h\, U^2 \geq (hU)^2/h$ so that $\beta_u \geq 1$.

The proposal in literature by Costa and Macedonio [2] for lava flows considered all the correction factors in the range 0.5–1.5, independently on their derivation. A value of $\beta_u < 1$ makes the PDE system non-hyperbolic, but our theorem is still valid provided that such a choice is balanced by a parameter $\beta_T \geq 1$ in order to verify assumption (i), even though this is not the case for the particular temperature profile we have assumed in §1.3.

For the time discretization of hyperbolic terms we will use higher-order methods belonging to the family of Strong Stability Preserving (SSP) Runge-Kutta (R-K) schemes, see §2.2. A similar positivity preserving property is proved for all these methods, since any SSP R-K method is expressible as a convex combination of intermediate Forward Euler steps, see Gottlieb et al. [35]. Hence, Theorem 2 can be applied to each step of the combination provided that Δt is sufficiently small (in order to satisfy the theorem assumption (ii) for each intermediate Euler method), ensuring the positivity preserving property for the whole SSP R-K method.

Remark 2. It is important to observe that, for each Euler term in the combination, the time step condition required by Theorem 2 depends on a, i.e. the maximum propagation velocity of the solution at interfaces evaluated at the considered term. Therefore the explicit determination of a global restriction for Δt (useful for the whole combination) is not so much simple, since we should estimate the evolution of a values during the intermediate steps of the R-K method.

2.2. Time discretization

In this section we present the Implicit-Explicit (IMEX) Runge-Kutta schemes proposed by Pareschi and Russo [34] used to solve the system (22). These methods have been developed to solve stiff systems of differential equations written in this form:

$$\frac{d}{dt}\mathbf{Q} = \mathcal{F}(\mathbf{Q}) + \mathbf{S}(\mathbf{Q}), \tag{32}$$

where $\mathbf{S}(\mathbf{Q})$ is the "stiff term". We write our problem in the same way by defining $\mathcal{F}(\mathbf{Q})$ as the spatial discretization of $-\partial_x \mathbf{f}(\mathbf{q}) + \mathbf{E}(\mathbf{q})$ in (20). In our situation the stiffness of $\mathbf{S}(\mathbf{Q})$ is due to the high viscosity, when $\gamma \gg 1$. In fact, the characteristic time of the source term is much smaller than the characteristic time of the advective part of the equations, hence the problem is said to be stiff and these kind of problems are generally difficult to solve numerically in an efficient way. A trivial solution is treating all the system explicitly and using a very small time step to ensure the stability of the scheme, but this approach results in long computational times.

In our scheme this limit has been overcome by applying an Implicit-Explicit method. An IMEX Runge-Kutta scheme consists of applying an implicit discretization to the stiff term and an explicit one to the non stiff terms. Applying the scheme to the system (32) we

obtain

$$\mathbf{Q}^{(l)} = \mathbf{Q}^n + \Delta t \sum_{k=1}^{l-1} \tilde{a}_{lk}\mathcal{F}(\mathbf{Q}^{(k)}) + \Delta t \sum_{k=1}^{\nu} a_{lk}\mathbf{S}(\mathbf{Q}^{(k)}), \quad l = 1, \ldots, \nu \tag{33}$$

$$\mathbf{Q}^{n+1} = \mathbf{Q}^n + \Delta t \sum_{k=1}^{\nu} \tilde{\omega}_k\mathcal{F}(\mathbf{Q}^{(k)}) + \Delta t \sum_{k=1}^{\nu} \omega_k\mathbf{S}(\mathbf{Q}^{(k)}). \tag{34}$$

The choice of the $\nu \times \nu$ matrices $\tilde{A} = (\tilde{a}_{lk})$, where $\tilde{a}_{lk} = 0$ for $l \geq k$, and $A = (a_{lk})$ and of the vectors $\tilde{\omega} = (\tilde{\omega}_1, \ldots, \tilde{\omega}_\nu)^T$ and $\omega = (\omega_1, \ldots, \omega_\nu)^T$ characterizes the different schemes.

The IMEX Runge-Kutta schemes is presented by a *double tableau* in the usual Butcher notation,

$$\begin{array}{c|c} \tilde{c} & \tilde{A} \\ \hline & \tilde{\omega}^T \end{array} \qquad \begin{array}{c|c} c & A \\ \hline & \omega^T \end{array}$$

where the coefficients $\tilde{c}$ and c, used for the treatment of non autonomous systems (which is not our case), are given by the usual relations

$$\tilde{c}_l = \sum_{k=1}^{l-1} \tilde{a}_{lk}, \qquad c_l = \sum_{k=1}^{l} a_{lk}$$

In all these schemes the implicit tableau corresponds to an L-stable scheme, that is $\omega^T A^{-1} e = 1$, where e is a vector whose components are all equal to 1. The notation (s, σ, p) is adopted to qualify the scheme, where s indicates the number of stages of the implicit scheme, σ the number of stages of the explicit scheme and p is the order of the IMEX scheme. Tables (12) report examples of schemes adopted for the proposed numerical simulations in Section §3.

Table 1: Tableau for the Explicit (left) Implicit (right) IMEX-SSP(2,2,1) R-K scheme

$$\begin{array}{c|cc} 0 & 0 & 0 \\ 1 & 1 & 0 \\ \hline & 1 & 0 \end{array} \qquad \begin{array}{c|cc} 0 & 0 & 0 \\ 1 & 0 & 1 \\ \hline & 0 & 1 \end{array}$$

The algebraic equations obtained at each step (which must be solved implicitly) are treated simply and efficiently by adopting diagonally implicit Runge-Kutta (DIRK) schemes ($a_{lk} = 0$, for $k > l$), that in addition guarantee that $\mathcal{F}$ is always evaluated explicitly.

20

Table 2: Tableau for the Explicit (left) Implicit (right) IMEX-SSP(3,3,2) R-K scheme, from Russo [23].

$$
\begin{array}{c|ccc}
0 & 0 & 0 & 0 \\
1/2 & 1/2 & 0 & 0 \\
1 & 1/2 & 1/2 & 0 \\
\hline
 & 1/3 & 1/3 & 1/3
\end{array}
\qquad
\begin{array}{c|ccc}
1/4 & 1/4 & 0 & 0 \\
1/4 & 0 & 1/4 & 0 \\
1 & 1/3 & 1/3 & 1/3 \\
\hline
 & 1/3 & 1/3 & 1/3
\end{array}
$$

Computation of the solution using IMEX DIRK schemes. When using DIRK schemes, at each internal Runge-Kutta step we have an implicit problem for all the cells of the domain. In fact, by applying a DIRK scheme to the ordinary differential equations (22) we obtain

$$
\mathbf{Q}_i^{(l)} = \mathbf{Q}_i^n + \Delta t \sum_{k=1}^{l-1} \tilde{a}_{lk} \left(-\frac{\mathbf{F}_{i+\frac{1}{2}}^{(k)} - \mathbf{F}_{i-\frac{1}{2}}^{(k)}}{\Delta x} + \mathbf{E}_i^{(k)} \right) + \Delta t \sum_{k=1}^{l} a_{lk} \mathbf{S}(\mathbf{Q}_i^{(k)}), \; l = 1, \ldots, \nu \quad (35)
$$

$$
\mathbf{Q}_i^{n+1} = \mathbf{Q}_i^n + \Delta t \sum_{k=1}^{\nu} \tilde{\omega}_k \left(-\frac{\mathbf{F}_{i+\frac{1}{2}}^{(k)} - \mathbf{F}_{i-\frac{1}{2}}^{(k)}}{\Delta x} + \mathbf{E}_i^{(k)} \right) + \Delta t \sum_{k=1}^{\nu} \omega_k \mathbf{S}(\mathbf{Q}_i^{(k)}). \quad (36)
$$

Furthermore $\mathbf{S}(\mathbf{Q}_i^{(k)})$ depends only on the solution in the cell i, thus, for each Runge-Kutta step, we have to solve n independent implicit problems, one for each cell of the domain.

All the implicit problems are solved by using a functional iterative method. For simplicity, we rewrite the equation (35) as follows:

$$
\mathbf{Q}_i^{(l)} = \mathbf{Q}_i^n + \Delta t \sum_{k=1}^{l-1} \tilde{a}_{lk} \left(-\frac{\mathbf{F}_{i+\frac{1}{2}}^{(k)} - \mathbf{F}_{i-\frac{1}{2}}^{(k)}}{\Delta x} + \mathbf{E}_i^{(k)} \right) + \Delta t \sum_{k=1}^{l-1} a_{lk} \mathbf{S}(\mathbf{Q}_i^{(k)}) + \Delta t \cdot a_{ll} \mathbf{S}(\mathbf{Q}_i^{(l)}),
$$

which is simply expressible as

$$
\mathbf{Q}_i^{(l)} - \Lambda_i - \Delta t \cdot a_{ll} \mathbf{S}(\mathbf{Q}_i^{(l)}) = 0 \quad \Longleftrightarrow \quad \Gamma(\mathbf{Q}_i^{(l)}) = 0
$$

where the term Λ_i contains the explicit part of the equation (35), which can be evaluated once during the iterative computation of the solution $\mathbf{Q}_i^{(l)}$.

We apply the Newton-Raphson method [36] to the problem $\Gamma(\mathbf{x}) = 0$ obtaining

$$
\begin{cases}
\mathbf{x}_{(0)} = \mathbf{Q}_i^n \\
\mathbf{x}_{(k+1)} = \mathbf{x}_{(k)} - J^{-1}_{|\mathbf{x}_{(k)}} \cdot \Gamma(\mathbf{x}_{(k)})
\end{cases}
\quad (37)
$$

where $J^{-1}_{|\mathbf{x}_{(k)}}$ is the inverse of the Jacobian of the function Γ evaluated at $\mathbf{x}_{(k)}$. The Newton-Raphson method is second order convergent, its computational cost depends on the cost of computing derivatives in the entries of the Jacobian and on the cost of the Jacobian inversion, in addition Newton-Raphson method suffers for a bad choice of the initial guess for the iterations. We underline here that the inversion of the Jacobian is not computationally expensive, since J is a $m \times m$ matrix, where m is the number of the equations having terms treated implicitly, for example in the 2D case $m = 3$.

2.2.1. Derivative approximation through complex numbers

The solution of the linear system appearing in (37) requires an accurate numerical evaluation of the Jacobian matrix J, i.e. the partial derivatives of Γ with respect to the components of $\mathbf{x}$. Due to the strong non-linearity of $\mathbf{S}(\mathbf{Q})$, it is not convenient to determine analytically the derivatives.

A common method to estimate the first derivative is the first-order forward-difference formula and higher order extensions which increase the stencil by using Taylor series expansion. However, when estimating sensitivities using finite-difference formulas we are faced with the "step-size dilemma", that is the desire to choose a small step size to minimize truncation error while avoiding the use of a step so small that errors due to subtracted cancellation become dominant.

A way to overcome this problem is to use complex functions. The first use of complex variables to estimate derivatives starts with the work of Lyness and Moler in 1967 [37, 38]. They introduced a reliable method for computing the derivatives of an analytic function, and later Squire and Trapp in 1998 [24] obtained a very simple expression for estimating the first derivative. It has been shown that this estimation is very accurate, extremely robust and easy to implement, with a reasonable computational cost. Recently it has been used for sensitivity analysis in computational fluid dynamics and further research on the subject has been carried out [39, 40, 41].

Through the complex-step derivative approximation we compute the Jacobian J, needed for the Newton-Raphson method, with an error of the same order of the machine working precision. All we have to do is to extend the function Γ to the complex plane, by introducing the new function $\tilde{\Gamma} : \mathbb{C} \to \mathbb{C}$ and to compute each column of the Jacobian at $\mathbf{x}$ as

$$J(\mathbf{x}) \cdot \mathbf{e}_j = \frac{\mathcal{I}(\tilde{\Gamma}(\mathbf{x} + i\, h\, \mathbf{e}_j))}{h} \tag{38}$$

where $(\mathbf{e}_j)_{j=1,\dots,m}$ are the canonical basis vectors, i denotes the imaginary unit and $\mathcal{I}(\cdot)$ stands for the imaginary part of a complex number.

3. Numerical simulations

The numerical code developed is a variant of the solver IMEX_SfloW2D [42] and it has been tested and validated with some literature examples and other tests to verify: (i) the well-balancing and the positivity preserving properties of the scheme; (ii) the consequences of using different limiters; (iii) the various behaviours when adopting constant vertical profiles of the variables or not. One recalls that in our scheme the linear reconstruction at interfaces is computed over the set of variables $\mathbf{P}$ (see §2.1) whereas in the scheme proposed by Kurganov and Petrova [17] it is computed over the variables $[w, hU, hV]$, hence we will stress over differences or similarities of such different computations; in the following, we indicate them with PVR and CVR respectively.

When the outputs of simulations done with different parameters or methods are compared, a metric is needed to compute the difference between two numerical solutions. Here,

if $\mathbf{y}^A$ and $\mathbf{y}^B$ are vectors containing solution values on the same grid, the following expression is used

$$diff(\mathbf{y}^A, \mathbf{y}^B) := \left[\Delta x \sum_i \left(\frac{|y_i^A - y_i^B|}{\max(|y_i^A|, |y_i^B|)} \right)^p \right]^{1/p} \tag{39}$$

with $p = 2$. This expression is a combination of the p-norm, recalled also by Leveque in 2004 [32], and the relative distance proposed by Ziv in 1982 [43].

The first and second tests are 1D dam-break simulations of viscous fluids over flat and inclined plane. We have doubled the experiments to present simulations both with high and low viscosity, in order to check the sensitivity of the scheme to the values of β_u, namely the sensitivity to constant or parabolic velocity profile. We remark that we use the terms high viscosity and low viscosity to distinguish between the two cases, but in all the examples the values of viscosity are large enough to result in laminar flows. In fact, the fluid simulated in the examples are representative of lava, silicone gum and silicone oil (both used in analogue experiments as benchmarks for models of lava flow emplacement). Moreover, the first test case sees also a temperature-dependent density simulation. In these tests, the spatial domain has been considered closed by fixed walls, hence homogeneous Dirichlet conditions have been imposed for the velocity (in this case zero velocity in correspondence to the walls) and homogeneous Neumann conditions for $h + B$ (zero gradient). The third and last test is a 2D simulation of a hot viscous fluid, and the focus is on the effects of a temperature-dependent viscosity. In this case we have modeled an open domain by imposing zero-gradient Neumann conditions both for velocities, $h + B$ and temperature. In order to preserve the positivity of the solution and the stability of the explicit scheme, associated with the CFL condition, a variable time step is used, which for the 1D simulations has been set to $\Delta t = k \frac{\Delta x}{a}$, with $k = 0.45$, while for the 2D simulations is given by $\Delta t = k \min \left\{ \frac{\Delta x}{a}, \frac{\Delta y}{b} \right\}$ with $k = 0.24$.

3.1. Dam-break of viscous fluids over a flat bottom.

We start from the simulations of viscous fluids with constant density. We explore the results focusing on some aims: (i) check the correct treatment of wet/dry states and of low/high viscosity; (ii) compare results (by computing the relative difference through Eq.(39)) obtained with PVR and CVR, 2 and 3 stages Runge-Kutta schemes reported in Tables 1-2 and constant and parabolic velocity profile; (iii) study the limiters effects. We conclude with the simulations of a temperature-dependent variable density fluid.

The dam-break test simulates the rupture of a dam: the viscous fluid is initially confined in a box and then, after the abrupt removal of one box sides, it starts to flow into a channel. This is a classical fluid mechanics problem, widely used because of its mathematical tractability and numerous applications, from hydraulic engineering, to food science, from geophysical science, to industrial problems [44]. This test is also considered as a standard measurement when characterizing fluid rheology, and it is a common benchmark for the shallow-water numerical codes too [45].

For our simulations, we consider a viscous fluid with a Newtonian rheology and a dam $L = 6.6\,\mathrm{m}$ long and $h = 1\,\mathrm{m}$ high over a horizontal domain of length $L_{TOT} = 75\,\mathrm{m}$, as suggested in [46] where the dam-break test is recommended as an isothermal benchmark for

lava-flow numerical codes. When the flow is slow enough to neglect inertia, it is possible to find analytic solutions. In such case, the results are comparable with the solution proposed by Saramito et al. [45] where the front evolution is described by a power law with exponent 0.5, for short times, and 0.2 for long times:

$$\frac{x_f(t)}{L} \approx \begin{cases} 0.284\left(\dfrac{t}{t_c}\right)^{1/2} & \text{if} \quad t < 2.5t_c \\[12pt] 1.133\left(\dfrac{t}{t_c} + 1.221\right)^{1/5} & \text{otherwise} \end{cases} \tag{40}$$

with the characteristic time t_c depending both on geometry of the initial condition and on fluid rheology: $t_c = \left(\dfrac{L}{h}\right)^2 \dfrac{\mu/\rho}{gh}$. In particular, the short term flow regimes is influenced by the fluid collapse immediately after the dam rupture and the fluid takes more time in propagating in this regime with the increase in viscosity. On the opposite, this sort of dynamics is almost instantaneous for a low viscosity fluid, moreover, in this case the gravity waves affect the propagation so that the equation (40) is no more able to describe such case.

We perform this test both with high and low viscosity, classifying the regime through the Froude number Fr defined by Eq. (18). For this application, we compute Fr using the front velocity of propagation and the mean thickness over the flow extent, as the front thickness is comparable with the mean value.

High viscosity. For the high-viscosity test, we model a silicone gum, following the laboratory dam-break experiment presented by Saramito et al. [45] where a transparent synthetic polymer SGM 36 manufactured by Dow Corning (USA) was employed. In this test temperature is not considered and we have used a constant kinematic viscosity value $\nu = \mu/\rho = 3.7\,\text{m}^2/\text{s}$ (as suggested in Example 1, Cordonnier et al. [46]).

The relative differences after $t = 100\,\text{s}$, anyway the velocity profile is chosen, between solutions computed by the PVR or CVR are very small ($\sim 10^{-4}$) and the same happens if we use R-K schemes with 2 or 3 stages ($\sim 10^{-7}$). In addition there are no appreciable differences in the solutions when using $\beta_u = 1$ or $\beta_u = 1.2$, i.e. constant or parabolic velocity profile, because the flow is in a strict subcritical regime with $Fr \approx 0.018$. This condition is mainly due to the high viscosity which, by opposing to the motion, keeps the flow velocity very low. Because of this, our results are comparable with the analytic solution of Eq. (40), see below.

In order to see the convergence behaviour, we compare results obtained with 200, 400, 800 and 3600 cells (using a 3-stages R-K, $\beta_u = 1$ and by PVR at interfaces) in Figure 3. We distinguish three different cases of computation of the interface values (see Eq. (23)): we have used both the *minmod* limiter, the *generalized minmod* limiter and also a piecewise constant reconstruction (namely no-limiter). We recall that the *generalized minmod* limiter is

$$\sigma_i^n = \text{minmod}\left(\theta\frac{Q_i^n - Q_{i-1}^n}{\Delta x}, \frac{Q_{i+1}^n - Q_{i-1}^n}{2\Delta x}, \theta\frac{Q_{i+1}^n - Q_i^n}{\Delta x}\right) \tag{41}$$

where the *minmod* function is defined as:

$$\text{minmod}\,(a_1, a_2, \dots) = \begin{cases} \min_j\{a_j\}, & \text{if} \quad a_j > 0 \quad \forall j, \\ \max_j\{a_j\}, & \text{if} \quad a_j < 0 \quad \forall j, \\ 0, & \text{otherwise} \end{cases}$$

By using the generalized minmod with $\theta = 2$ a very accurate solution is obtained with 400 cells whereas, with the minmod limiter, similar results are obtained with 800 cells and, in the case of no limiter, with 3200 cells. On the opposite, by using the generalized minmod limiter a less refined grid is sufficient to obtain a very good solution.
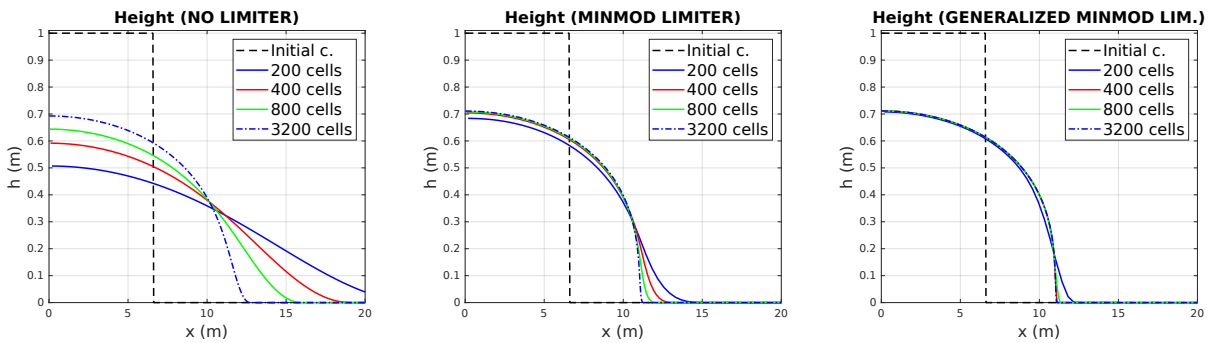
Figure 3: *Dam-break of a viscous fluid over a flat bottom.* Solution at $t = 100\,\text{s}$ of a high-viscosity fluid. Solutions computed by different grid size over a domain $75\,\text{m}$ long. *Left*: no limiter. *Center*: minmod limiter. *Right*: generalized minmod limiter.

Figure 4 shows the convergence to the analytical solution of the front position, see Eq. (40). Three different grid resolutions have been used: 400, 800 and 1600 cells, and the generalized minmod limiter has been adopted. The front position of the numerical solutions is determined by a threshold value $h = 10^{-3}\,\text{m}$.

For the 400 cells grid, the simulation with PVR, generalized minmod limiter and $k = 0.45$ for the time step condition, took 3432 time steps with a total execution time of $7.91\,\text{s}$, whereas the time-step size grew slowly up to $3.2 \cdot 10^{-2}\,\text{s}$.

Low viscosity. For the low-viscosity test, we model a silicone oil, the material used by Lister [47] in his laboratory experiments for the spreading of isothermal viscous fluids on a plane. This silicone oil is characterized by a kinematic viscosity $\nu = \mu/\rho = 1.16 \cdot 10^{-3}\,\text{m}^2/\text{s}$ (taken from Example 2, Cordonnier et al. [46]). Also for this test, temperature is not considered.

One observes a low sensitivity to most numerical parameters. Regardless of the assumption about the velocity profile, the relative differences between solutions obtained with R-K schemes with 2/3 stages and PVR/CVR are about 10^{-3}. The results are also independent from the limiter adopted. On reverse, the assumption of constant or parabolic velocity profiles leads to different dynamics, as shown in Figure 5. The main outcome of the two simulations is that solutions with different vertical profiles have distinct shapes and temporal evolution, indeed initially the flow front of the simulation with $\beta_u = 1.2$ (parabolic profile)
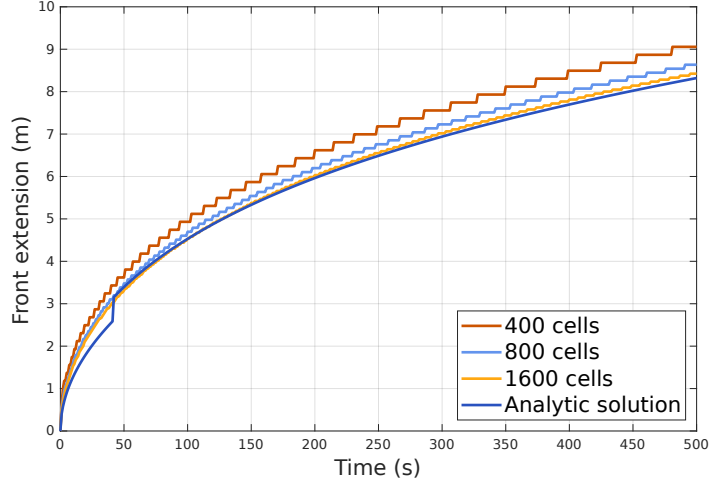
Figure 4: *Dam-break of a viscous fluid over a flat bottom.* Front position over time: analytic solution given by Eq. (40) and simulation results obtained with different grid size.
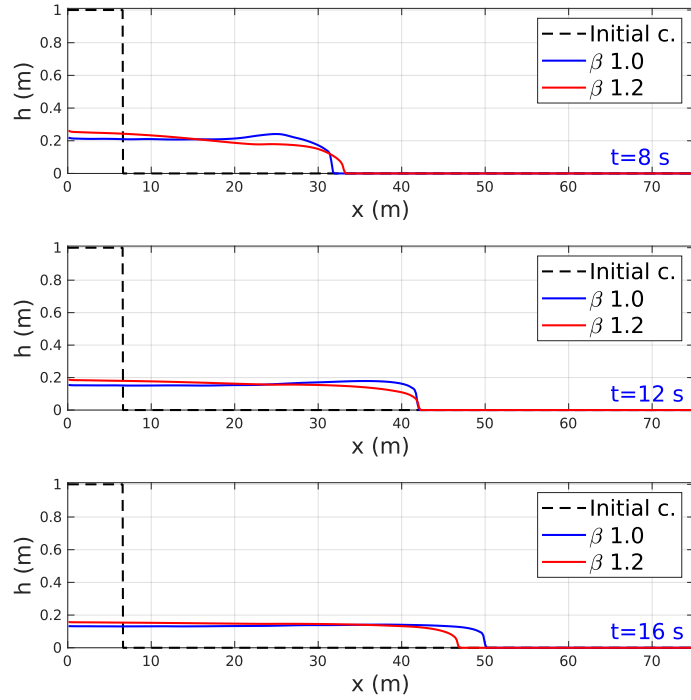

Figure 5: *Dam-break of a viscous fluid over a flat bottom.* Evolution: *top* $t = 8$ s, *center* $t = 12$ s, *bottom* $t = 16$ s of a low-viscosity fluid, computed by PVR at interfaces with the minmod limiter, 3 stages IMEX R-K scheme. Comparison between $\beta_u = 1.0$ and $\beta_u = 1.2$ (constant and parabolic velocity profile).

proceeds faster, after 12 s the solutions are equal merit and then they reverse positions (see Figure 5).

The sensitivity to the velocity vertical profile emerges because, in this case, the flow

26

regime is supercritical, therefore the inertial forces control the flow dynamics and the influence of the β_u coefficient becomes notable. In this case there is no analytical solution for comparison and Eq. (40) is not applicable. Figure 6, representing the front position and the Froude number, shows that differences in the Froude numbers between the two simulations result in diverse velocities of propagation of the flow front.
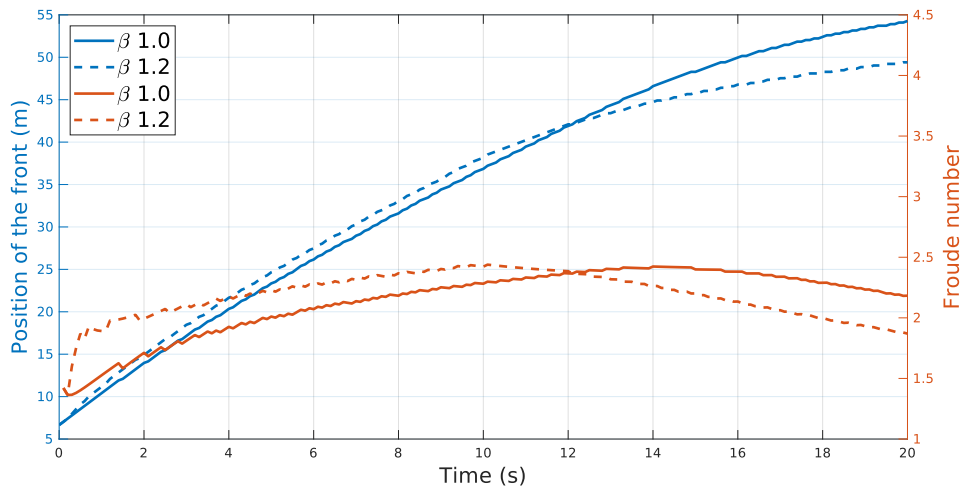

Figure 6: *Dam-break of a viscous fluid over a flat bottom.* Evolution of the front position (blue) and the Froude number (red). Comparison between constant velocity profile with $\beta_u = 1.0$ (solid line) and parabolic velocity profile $\beta_u = 1.2$ (dashed line).

With respect to the high-viscosity case, the low-viscosity test highlights a lower sensitivity of the numerical solution to the choice of the limiter, as shown by Figure 7. In addition, there is no necessity to refine too much the discretized domain since the solutions computed with only 400 cells are all close to the convergence solution.

Using a 400 cells grid, for the simulation with PVR, with the generalized minmod limiter and with $k = 0.45$ for the time step condition, in the case of $\beta_u = 1$ (constant velocity profile) we needed 597 time steps with a total execution time of 1.9 s whereas the time-step size grew slowly up to $2.1 \cdot 10^{-2}$ s; in the case of $\beta_u = 1.2$ (parabolic velocity profile), we needed 757 time steps with a total execution time of 2.44 s whereas the time-step size grew slowly up to $1.9 \cdot 10^{-2}$ s.

Low viscosity with temperature dependent density. Silicon oil, the material employed in the previous low-viscosity test, is characterized by a linear dependence of density on temperature in the range of $300 - 380$ K, as supported from paper [48]. That work presented some experimental data about mineral oil and silicone oil and we have extrapolated from it the values for the linear relation between density and temperature, Eq. (14), $\rho(T) = 1200 - 0.75T$. We set the maximum temperature on the surface $T_1 = 338$ K and the initial depth-averaged temperature $T = 330$ K with the thermal boundary layer thickness $\delta_T = h/4$. In Figure 8 we present the results of the simulation at time $t = 8$ s and 20 s computed with 400 cells by PVR at interfaces with the minmod limiter, 3 stages IMEX R-K scheme, $\beta_u = 1.2$
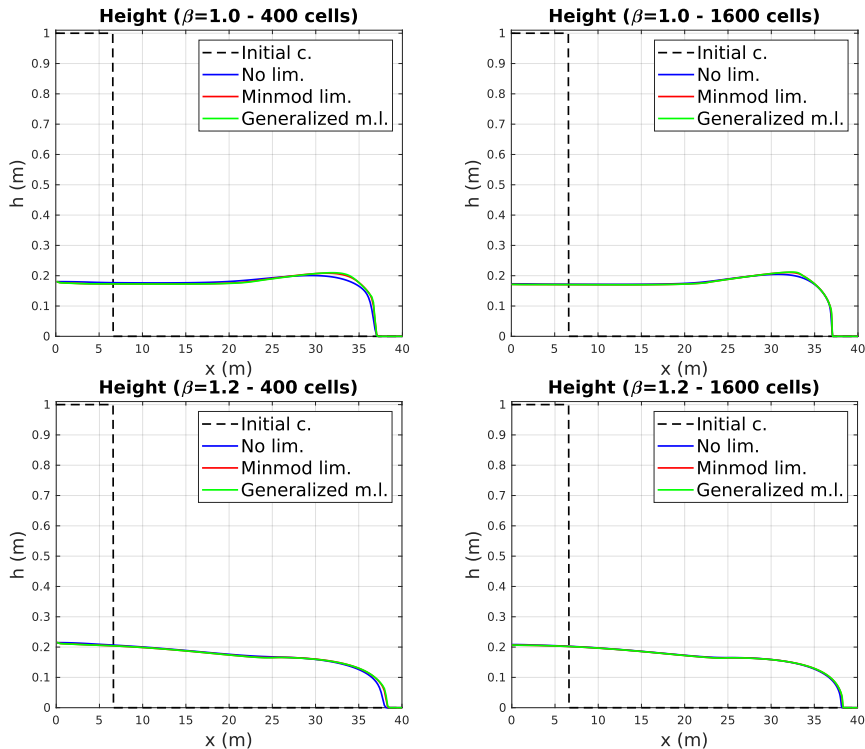
Figure 7: *Dam-break of a viscous fluid over a flat bottom.* Solutions at $t = 10\,\text{s}$ of a low-viscosity fluid computed without limiter, with the minmod and the generalized minmod limiter. *Top:* $\beta_u = 1.0$. *Bottom:* $\beta_u = 1.2$.

(parabolic velocity profile). Since we consider a laminar flow, the co-presence of velocity profile and thermal profile results that the top layer with the highest temperature moves faster than the lower part and it rapidly constitutes a large portion of the front. For this reason the front has the highest temperature and consequently the lowest density; conversely, the tail average temperature decreases and then density grows.

The relative difference between the variable-density and the constant-density solutions increases with time reaching the maximum value $\sim 10^{-1}$ at $t = 10$s. The simulation results highlight that, in this circumstance, density variations do not affect significantly nor the front position neither the global shape of the flow, therefore in the following tests we neglect density variations.

3.2. Dam-break of viscous fluids over an inclined bottom.

The purposes of this second test are analogue to those of the previous one: (*i*) check the correct treatment of wet/dry states and low/high viscosity; (*ii*) compare the solutions (by computing the relative difference with Eq.(39)) obtained with constant and parabolic velocity profile, PVR and CVR and 2 and 3 stages Runge-Kutta schemes, as reported in Tables 1–2; (*iii*) study the limiters effects.

The dam-break setting is like to that of the former case §3.1, but the horizontal plane is inclined at a slope of 2.5° from horizontal.
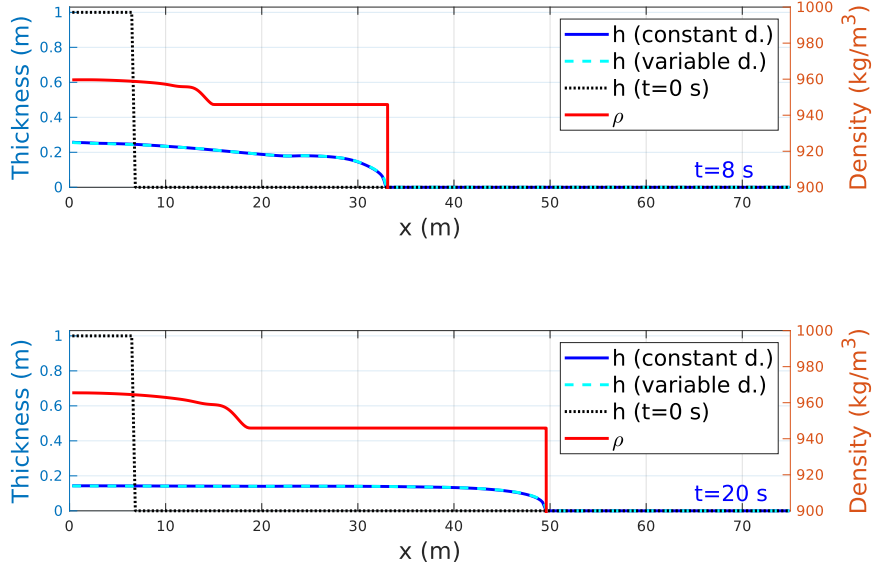
Figure 8: *Dam-break of a viscous fluid over a flat bottom.* Thickness and density for solutions of a low-viscosity fluid with temperature-dependent variable density and constant density. Simulation computed over 400 cells by PVR at interfaces with the minmod limiter, 3 stages IMEX R-K scheme, $\beta_u = 1.2$ (parabolic velocity profile). *Top: $t = 8$ s. Bottom: $t = 20$ s.*

High viscosity. For the high-viscosity test we have considered again a silicone gum in isothermal condition, with a kinematic viscosity $\nu = \mu/\rho = 3.7\,\mathrm{m^2/s}$ (as suggested in [46]).

After $t = 100$ s, for both the constant and parabolic velocity profiles, the relative difference between results computed with PVR and CVR is small ($\sim 10^{-4}$) and that calculated between solutions obtained with 2 and 3 R-K stages is even smaller ($\sim 10^{-7}$). In Figure 9 the high sensitivity to different limiters is very clear, and once more the generalized minmod limiter with $\theta = 2$ is confirmed to produce better approximations even with a less refined grid.

As in the previous test with high-viscosity conditions, the Froude number is very small $Fr \approx 0.023$. In such subcritical regime situation, the inertial forces are minor compared to gravitational and viscous forces and the effect of the vertical velocity profiles on flow dynamics is negligible. Indeed, results obtained with $\beta_u = 1$ or $\beta_u = 1.2$ are similar, with a relative difference of the order of 10^{-6}. In this test, the value of Fr is obtained again by using the front velocity propagation and the mean thickness over the flow extent, since the front thickness is comparable with the mean value.

Using a 400 cells grid, for the simulation with PVR, the generalized minmod limiter and $k = 0.45$ for the time step condition, we needed 3265 time steps with a total execution time of 7.95 s, whereas the time-step size grew up slowly and reached the maximum value of $3.4 \cdot 10^{-2}$ s.

Low viscosity. For the low-viscosity test, we model again a silicone oil with the kinematic viscosity $\nu = \mu/\rho = 1.16 \cdot 10^{-3}\,\mathrm{m^2/s}$ (taken from [46]). Also for this test, temperature is not considered.
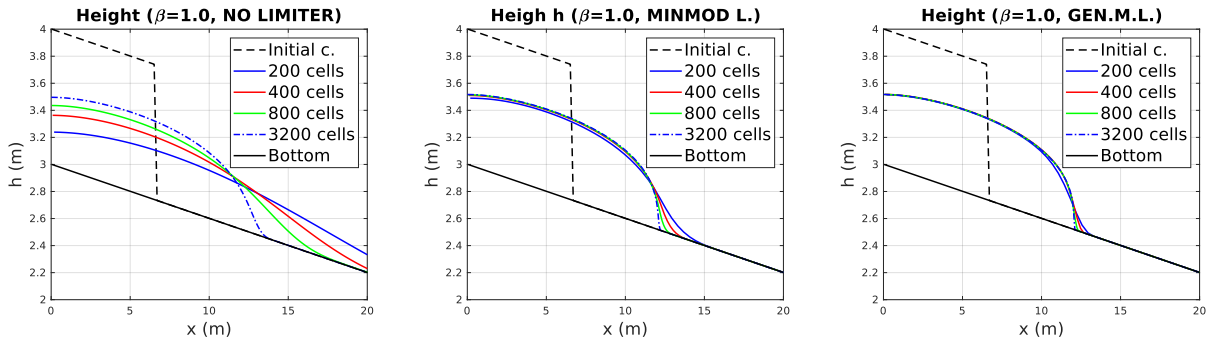
29

Figure 9: *Dam-break of a viscous fluid over an inclined bottom.* Solution at $t = 100$s for a high-viscosity fluid. Comparison between solutions computed with different grid size over a domain 75m long. *Left*: no limiter. *Center*: minmod limiter. *Right*: generalized minmod limiter.

At $t = 10$ s, regardless of the assumption about the velocity profile, the relative distance between simulations computed with R-K scheme with 2 and 3 stages is about 10^{-3}; whereas, comparing CVR and PVR, the relative distance is one order of magnitude larger; moreover, there is no sensitivity to the limiter adopted.

For a fixed limiter and a fixed number of Runge-Kutta stages, there is a great difference in solutions with constant and parabolic velocity profile, $\beta_u = 1$ and $\beta_u = 1.2$ respectively, as shown in Figure 10. In particular, at $t = 5$ s the runout of the simulation with $\beta_u = 1.2$ is larger than that obtained with $\beta_u = 1$, whereas at $t = 10$ s the opposite occurs. The sensitivity to the velocity profile assumption finds correspondence in the supercritical regime situation, shown by the Froude number reported in Figure 10. Indeed, in such cases, after the initial collapse, the inertial force dominates the dynamics and then the effects of different values of β_u are considerable, as already observed in the former low-viscosity case in §3.1. In this case, the value of Fr is computed using the front velocity of propagation and the flow thickness averaged over the 10 m close to the front, avoiding the thin tail.

Furthermore, one observes that the tail does not move down the slope with time. This happens because of the rheological model adopted, with the friction force inversely proportional to h; for this reason, when the tail thickness decreases, the viscosity increases and hence the velocity tends to zero.

Using a 400 cells grid, the simulation with PVR, generalized minmod limiter and with $k = 0.45$ at the time step condition, in the case of $\beta_u = 1$ (constant velocity profile) took 751 time steps with a total execution time of 2.65 s whereas the time-step size has grown up to $1.4 \cdot 10^{-2}$s; in the case of $\beta_u = 1.2$ (parabolic velocity profile) the simulation took 972 time steps with a total execution time of 2.65 s whereas the time-step size grew increased till $1.2 \cdot 10^{-2}$s.

3.3. 2D Simulation of a temperature-dependent viscous fluid

This last test is a 2D simulation of a temperature-dependent viscous fluid. Our aim is to check the coupling between momentum and temperature equations, and the effects of a Newtonian rheology.
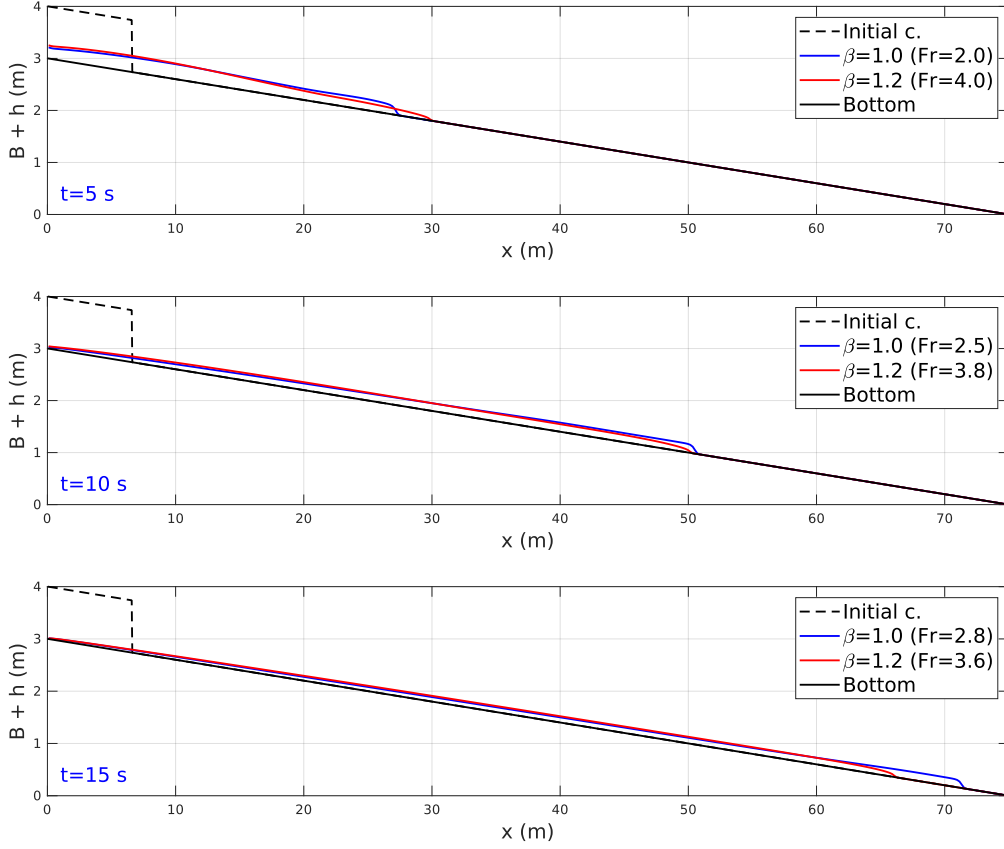
Figure 10: *Dam-break of a viscous fluid over an inclined bottom.* Evolution: *top* $t = 5$ s, *center* $t = 10$ s, *bottom* $t = 15$ s of a low-viscosity fluid, computed by PVR at interfaces with the minmod limiter, 3 stages IMEX R-K scheme. Comparison between $\beta_u = 1.0$ and $\beta_u = 1.2$, i.e. constant and parabolic velocity profile. The Froude number Fr points out a supercritical regime in both conditions; its trend increases for $\beta_u = 1.0$, while it is decreasing for $\beta_u = 1.2$.

The fluid is initially concentrated in a hemispherical shape over a 35° inclined flat plane, then it slides down over such plane which merges continuously into a horizontal plane, passing through a smooth transition zone. The initial conditions and the topography of this test are similar to that used in Example 4.1 from Wang et al. [49]. The computational domain is a rectangle 30 m long and 20 m wide and the inclination angle is defined as

$$\alpha(x) = \begin{cases} 35°, & 0 \leq x < 17.5, \\ 35°(1 - (x - 17.5)/4), & 17.5 \leq x < 21.5, \\ 0°, & 21.5 \leq x \leq 30. \end{cases}$$

In this test we use viscosity values and temperature values representative of lava flows. We also consider a temperature-dependent viscosity adopting an exponential relationship as the one suggested by Costa and Macedonio [2]

$$\gamma = \frac{3\,\nu(T)}{h}, \quad \nu(T) = \nu_r \exp[-b(T - T_r)],$$

31

where b is an appropriate rheological parameter and ν_r is the reference kinematic viscosity that the fluid has at the reference temperature T_r. Initially, the depth-averaged temperature and the reference temperature are set equal ($T = T_r = 1353$ K), hence viscosity coincides with the reference viscosity.

The domain is discretized by 80×54 cells. The PVR is used at the interfaces with the generalized minmod limiter ($\theta = 1.3$) and with a 3 stages IMEX R-K scheme for time marching, see Table 2. For the characteristic thermal boundary-layer, we adopt two thickness values $\delta_T = h/n$ with $n = 4$ and $n = 10$, which lead to different values for β_T and β_{T_1}:

$$\beta_T = \begin{cases} 0.234375, & n = 4, \\ 0.0975, & n = 10, \end{cases} \qquad \beta_{T_1} = \begin{cases} 0.765626, & n = 4, \\ 0.9025, & n = 10. \end{cases}$$

One reminds that the presence of non trivial values for β_T and β_{T_1} depends on the fact that we have considered a parabolic velocity profile, therefore in these cases $\beta_u = 1.2$ must be set, otherwise the model would lose its consistency.

High viscosity. We have adopted again the value $\nu_r = 3.7\,\mathrm{m}^2/\mathrm{s}$ (taken from Example 1, Cordonnier et al. [46]) for the kinematic viscosity. In Figure 11 we compare, for $n = 4$, results obtained at time $t = 600\,\mathrm{s}$ with constant and variable temperature profiles, respectively, while in Figure 12 we present the time evolution of their contour. For this viscosity value, the differences between solutions obtained with $n = 4$ or 10 are negligible, thus the results of the latter case are not shown.
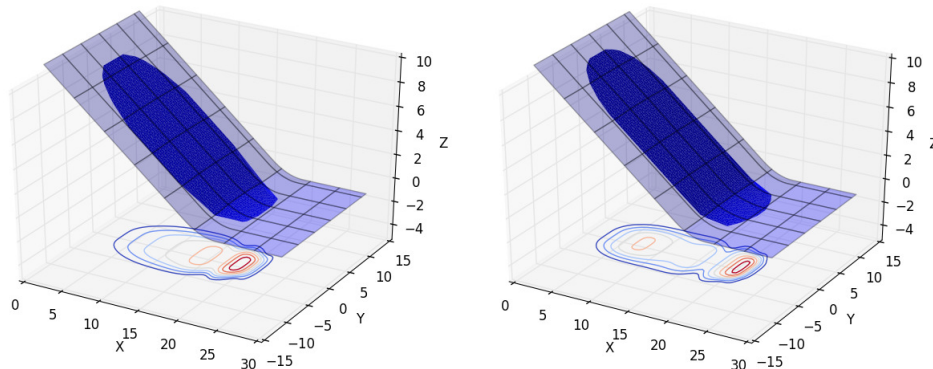

Figure 11: *2D Simulation of a temperature-dependent viscous fluid.* Comparison of high-viscosity fluid simulations computed with different thermal profiles, at $t = 600\,\mathrm{s}$: *left* constant with $T_1 = 1353\,\mathrm{K}$, *right* piecewise linear with $T_1 = 1400\,\mathrm{K}$.

When a constant temperature profile is assumed ($T_1 = T = T_r$), T is simply advected with the flow and the kinematic viscosity equals the reference value ν_r. If the piecewise linear temperature profile is considered, the maximum temperature is set higher than the averaged temperature ($T_1 = 1400\,\mathrm{K}$) and then T changes (both in space and in time) during the simulation. In the latter case, due to velocity and thermal profiles, the top layer has the highest temperature and moves with a speed larger than the lower part, hence it propagates

faster arriving soon to constitute the front; on the contrary, the fluid at the upper part of the plane becomes, on average, colder. In this situation, at time $t = 600\,\mathrm{s}$, the depth-averaged temperature reaches the minimum $T = 1247\,\mathrm{K}$ at the upper part of the plane, approximately at $x \approx 4.5\,\mathrm{m}$; such minimum leads to a kinematic viscosity value higher than the reference one, and in this situation an amount of fluid is accumulated at the upper part of the plane, whereas in the case of constant thermal profile this little pile does not remain.

For $600\,\mathrm{s}$ of simulation, with $k = 0.24$ for the time step condition, the constant temperature profile case, the computation needed 9583 time steps, a total execution time of $547.06\,\mathrm{s}$, while the time-step size reached the maximum value of $7.3 \cdot 10^{-2}\,\mathrm{s}$. Whereas, the case of piecewise linear temperature profile needed 8804 time steps, a total execution time of $522.83\,\mathrm{s}$, and the time-step size reaches the maximum value of $7.9 \cdot 10^{-2}\,\mathrm{s}$.
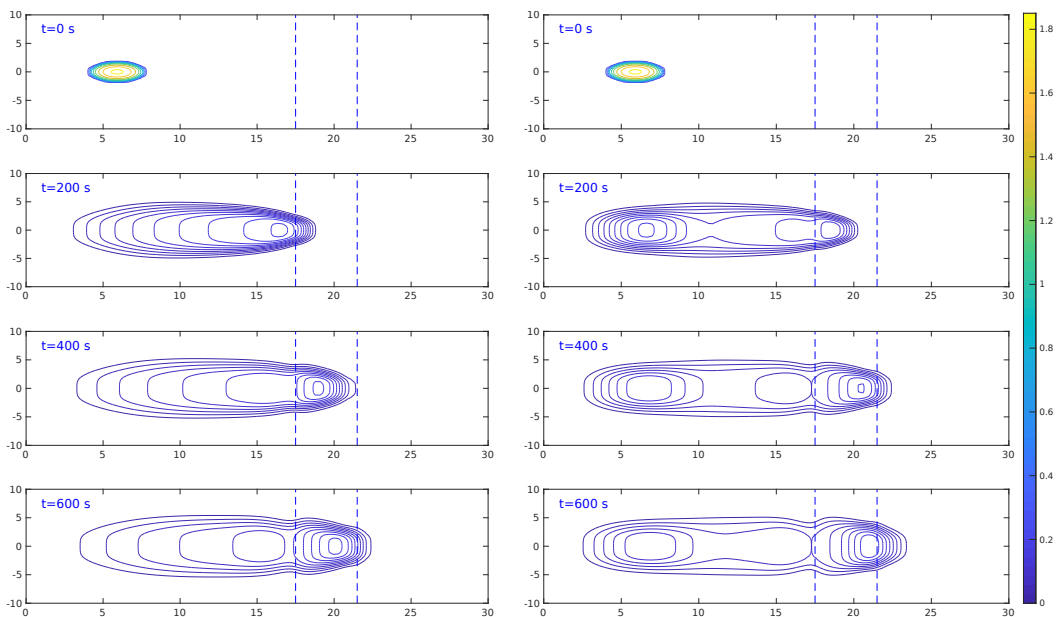

Figure 12: *2D Simulation of a temperature-dependent viscous fluid.* Evolution of high-viscosity fluid simulations computed with different thermal profiles: *left* constant profile with $T_1 = 1353\,\mathrm{K}$, *right* piecewise linear profile and $T_1 = 1400\,\mathrm{K}$. The section between the two dotted lines is the transition zone from the inclined plane to the horizontal plane.

Low viscosity. For the low-viscosity test, we used again the value $\nu_r = 1.16 \cdot 10^{-3}\,\mathrm{m^2/s}$ for the kinematic viscosity (taken from [46]).

We start comparing solutions obtained by different characteristic thermal boundary layers δ_T/n, with $n = 10$ and $n = 4$, and with the maximum temperature on the surface as $T_1 = 1400\,\mathrm{K}$, see Figure 13. When $n = 10$ the fluid propagates faster because the top layer with the maximum temperature is thicker, therefore the averaged temperature is greater and the kinematic viscosity lower. However, as in the former high-viscosity case, there is a little pile of matter in the upper part of the plane. The computation of $3\,\mathrm{s}$ of simulations
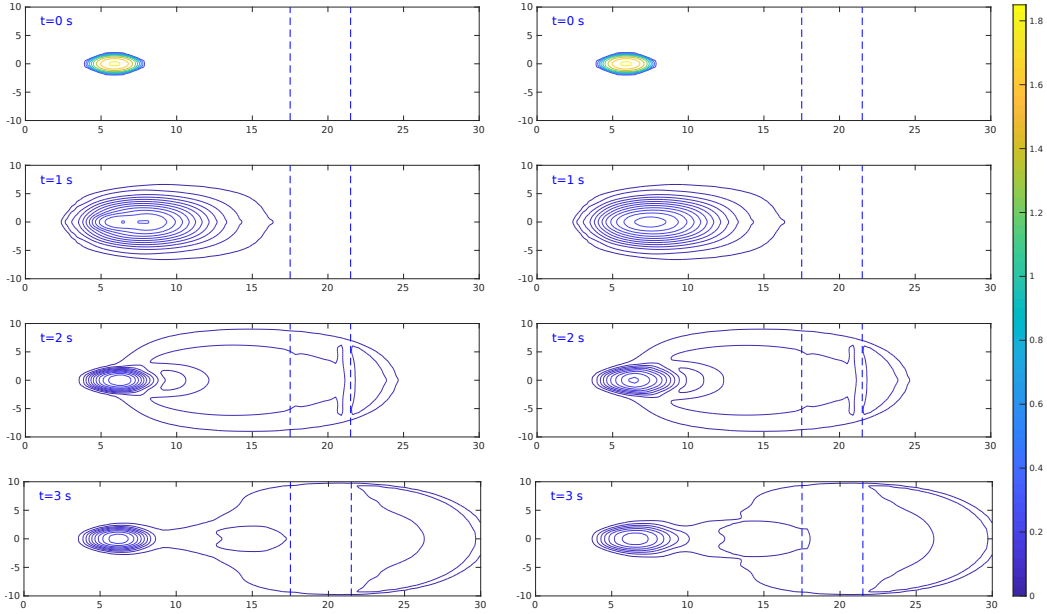
Figure 13: *2D Simulation of a temperature-dependent viscous fluid.* Evolution of a low-viscosity fluid with temperature-dependent viscosity computed with different characteristic thermal boundary layer $\delta_T = h/n$: *left* $n = 10$, *right* $n = 4$. The section between the two dotted lines is the transition zone from the inclined plane to the horizontal plane.

in both cases of $n = 4$ and $n = 10$, with $k = 0.24$ for the time step condition, required 552 time steps and 28.89 s, while the time step size reached the maximum value $1.1 \cdot 10^{-2}$ s.

We conclude with simulations with a simple transport of temperature and a temperature independent viscosity, in which we compare solutions with different velocity profiles (as in the previous 1D tests). A constant temperature profile and a constant kinematic viscosity are assumed by setting $T_1 = T = T_r = 1353$ K. We find, once more, that with a constant profile the fluid propagates faster and the front is thicker, see Figure 14. For 3 s of simulation, with $k = 0.24$ for the time step condition, the case of a parabolic velocity profile needed 502 time steps with a total execution time of 24.18 s, whereas the time-step size has reached the maximum value of 10^{-2} s; instead, the case of a constant velocity profile took 353 time steps with a total execution time of 16.69 s, whereas the time-step size has reached the maximum value of $1.2 \cdot 10^{-2}$ s.

4. Concluding remarks

In this work we studied a modified shallow water model for laminar viscous fluid with non-constant vertical profiles for velocity and temperature. We presented a second-order well-balanced and positivity preserving spatial discretization scheme for its solution, based on the work of Kurganov and Petrova [17], coupled with an implicit-explicit Runge-Kutta technique for the temporal discretization. The implicit treatment of stiff terms, required to properly model the behaviour of laminar viscous flows, was obtained by computing the
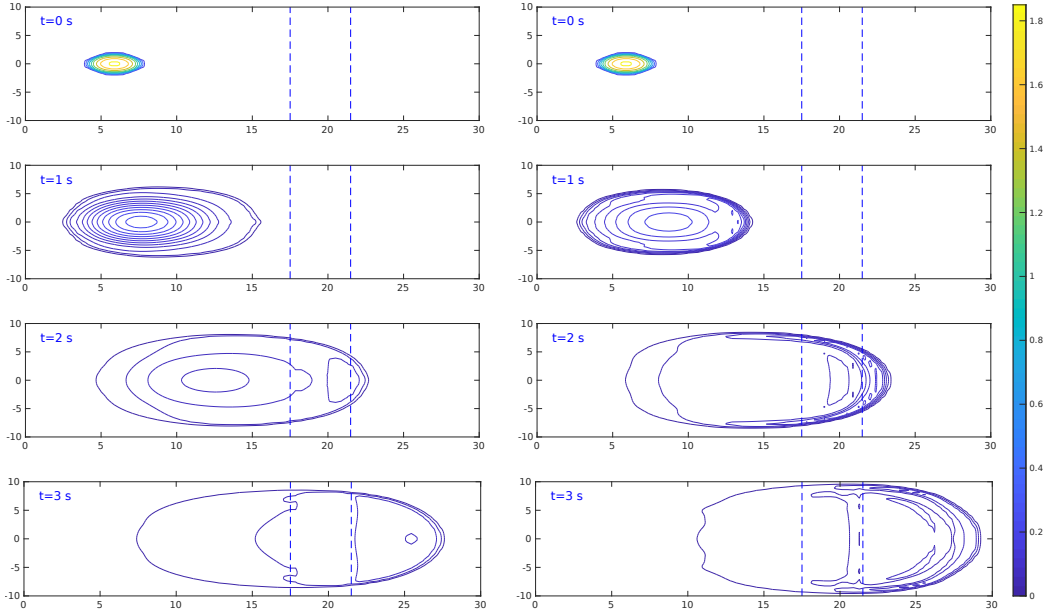
34

Figure 14: *2D Simulation of a temperature-dependent viscous fluid.* Evolution of a low-viscosity fluid with viscosity not temperature dependent with different vertical velocity profile: *left* parabolic profile, hence $\beta_u = 1.2$, *right* constant profile, hence $\beta_u = 1.0$. The section between the two dotted lines is the transition zone from the inclined plane to the horizontal plane.

Jacobians of the fluxes with complex arithmetic.

We have shown that a geometrical limiter adoption produces a better accuracy in results for all the test performed, but high-viscosity fluids are more sensitive to the limiter chosen in terms of diffusive behaviour (see in particular the first and second test cases which show the dynamics of a viscous fluid over a flat or inclined plane respectively). The main differences when considering constant or parabolic velocity profiles have been observed for supercritical regimes (mainly associated with simulations of low-viscosity fluids); in particular, in the case of constant velocity profile the fluid propagates faster than in the other case on the long time. Similar differences are appreciated in the last test (2D simulation of a viscous fluid over an inclined plane), where viscosity is temperature dependent so that the combined effects of temperature and velocity profiles are evident. Finally, we have shown that computing interface reconstructions over the set of variables $\mathbf{P} = [w, U, V, T]$ produces in general very similar results to those obtained by using the variables $[w, hU, hV]$, and allows to avoid the process of desingularization to obtain the flow velocities at the interfaces.

The work presented in this article sets the basis for advances in some specific applied fields, for instance lava flow simulations, where we plan future developments. In that context, the temperature equation can be enriched by other source terms accounting for the thermal exchanges between lava, the environment and the ground such as radiative, convective and conductive phenomena [2], whereas the rheological model can be modified to consider crystallization occurring with cooling.

References

[1] M. .F Sheridan, A. J. Stinton, A. Patra, E. B. Pitman, A. Bauer, and C. C. Nichita. Evaluating Titan2D mass-flow model using the 1963 Little Tahoma peak avalanches, Mount Rainier, Washington. *Journal of volcanology and geothermal research*, 139(1-2):89–102, 2005.

[2] A. Costa and G. Macedonio. Numerical simulation of lava flows based on depth-averaged equations. *Geophysical Research Letters*, 32(5), 2005.

[3] K. Kelfoun and S. V. Vargas. VolcFlow capabilities and potential development for the simulation of lava flows. *Geological Society, London, Special Publications*, 426(1):337–343, 2016.

[4] J. N. Procter, S. J. Cronin, I. C. Fuller, M. Sheridan, V. E. Neall, and H. Keys. Lahar hazard assessment using Titan2D for an alluvial fan with rapidly changing geomorphology: Whangaehu River, Mt. Ruapehu. *Geomorphology*, 116(1-2):162–174, 2010.

[5] D. L. Williamson, J. B. Drake, J. J Hack, R. Jakob, and P. N. Swarztrauber. A standard test set for numerical approximations to the shallow water equations in spherical geometry. *Journal of Computational Physics*, 102(1):211–224, 1992.

[6] J. Behrens. Atmospheric and ocean modeling with an adaptive finite element solver for the shallow-water equations. *Applied Numerical Mathematics*, 26(1-2):217–226, 1998.

[7] F. Lyard, F. Lefevre, T. Letellier, and O. Francis. Modelling the global ocean tides: modern insights from FES2004. *Ocean dynamics*, 56(5-6):394–415, 2006.

[8] C. L. Mader. *Numerical modeling of water waves*. CRC press, 2004.

[9] E. D. Fernández-Nieto, F. Bouchut, D. Bresch, M. J. C. Diaz, and A. Mangeney. A new Savage-Hutter type model for submarine avalanches and generated tsunami. *Journal of Computational Physics*, 227(16):7720–7754, 2008.

[10] J. Boussinesq. *Essai sur la théorie des eaux courantes*. Impr. nationale, 1877.

[11] A. J. Hogg and D. Pritchard. The effects of hydraulic resistance on dam-break and other shallow inertial flows. *Journal of Fluid Mechanics*, 501:179–212, 2004.

[12] S. F. Bradford and B. F. Sanders. Finite-volume model for shallow-water flooding of arbitrary topography. *Journal of Hydraulic Engineering*, 128(3):289–298, 2002.

[13] A. Kurganov and D. Levy. Central-upwind schemes for the Saint-Venant system. *ESAIM: Mathematical Modelling and Numerical Analysis*, 36(3):397–425, 2002.

[14] S. Bi, J. Zhou, Y. Liu, and L. Song. A finite volume method for modeling shallow flows with wet-dry fronts on adaptive cartesian grids. *Mathematical Problems in Engineering*, 2014, 2014.

[15] L. Begnudelli and B. F. Sanders. Conservative wetting and drying methodology for quadrilateral grid finite-volume models. *Journal of Hydraulic Engineering*, 133(3):312–322, 2007.

[16] Q. Liang and A. G. L. Borthwick. Adaptive quadtree simulation of shallow flows with wet–dry fronts over complex topography. *Computers & Fluids*, 38(2):221–234, 2009.

[17] A. Kurganov and G. Petrova. A second-order well-balanced positivity preserving central-upwind scheme for the Saint-Venant system. *Commun. Math. Sci.*, 5(1):133–160, 2007.

[18] X. Liu, J. Albright, Y. Epshteynb, and A. Kurganov. Well-balanced positivity preserving central-upwind scheme with a novel wet/dry reconstruction on triangular grids for the Saint-Venant system. *Journal of Computational Physics*, 374:213–236, 2018.

[19] X. Liu. A robust numerical model for shallow water governing solute transport with wet/dry interfaces. *Comput. Methods Appl. Mech. Engrg.*, 351:85–108, 2019.

[20] F. Bouchut. *Nonlinear stability of finite Volume Methods for hyperbolic conservation laws: And Well-Balanced schemes for sources*. Springer Science & Business Media, 2004.

[21] R. Manning, J. P. Griffith, T. F. Pigot, and L. F. Vernon-Harcourt. *On the flow of water in open channels and pipes*. 1890.

[22] G. Russo. Central schemes for balance laws. In Freistühler H., Warnecke G., editor, *Hyperbolic Problems: Theory, Numerics, Applications*, ISNM International Series of Numerical Mathematics, 2001.

[23] G. Russo. Central schemes for conservation laws with application to shallow water equations. In Romano G. (eds) Rionero S., editor, *Trends and Applications of Mathematics to Mechanics*, pages 225–246. The organization, Springer, 2005.

[24] W. Squire and G. Trapp. Using complex variables to estimate derivatives of real functions. *Siam Review*, 40(1):110–112, 1998.

[25] M. J. Castra Día, E. D. Fernández-Nieto, and A.M. Ferreiro. Sediment transport models in hallow water equations and numerical approach by high order finite volume methods. *Computers & Fluids*, 37(3):299–316, 2008.

[26] S. Li and C. J. Duffy. Fully-coupled modeling of shallow water flow and pollutant transport on unstructured grids. *Procedia Environmental Sciences*, 13(3):2098–2121, 2012.

[27] M. de' Michieli Vitturi, T. Esposti Ongaro, G. Lari, and A. Aravena. IMEX_SfloW2D 1.0. a depth-averaged numerical flow model for pyroclastic avalanches. *Geosci. Model Dev. Discuss.*, 2018.

[28] A. Wirth. A guided tour through physical oceanography. *Physical Oceanography*, 2015.

[29] I. M. Krieger and T. J. Dougherty. A mechanism for non-newtonian flow in suspensions of rigid spheres. *Transactions of the Society of Rheology*, 3(1):137–152, 1959.

[30] M. Dragoni, I. Borsari, and A. Tallarico. A model for the shape of lava flow fronts. *Journal of Geophysical Research: Solid Earth*, 110(B9), 2005.

[31] J. Gerbeau and B. Perthame. Derivation of viscous Saint-Venant system for laminar shallow water: Numerical validation. *Discrete and continuous dynamical systems–series B*, 1(1):89–102, 02 2001.

[32] R. J. LeVeque. *Finite volume methods for hyperbolic problems*. Cambridge Texts in Applied Mathematics, 2004.

[33] E. F. Toro. The dry bed problem in shallow water flows. *College of aeronautics, Report No. 9007*, 1990.

[34] L. Pareschi and G. Russo. Implicit-Explicit Runge-Kutta schemes for stiff system of differential equations. In *Recent trends in numerical analysis*, pages 269–288. Nova Science, 2000.

[35] S. Gottlieb, C. W. Shu, and E. Tadmor. Strong stability-preserving high order time discretization methods. *SIAM Review*, 43:89–112, 2001.

[36] J. M. Ortega and W. C. Rheinboldt. *Iterative Solution of Nonlinear Equations in Several Variables*. Cambridge university, 1987.

[37] J. N. Lyness and C. B. Moler. Numerical differentiation of analytic functions. *SIAM Journal on Numerical Analysis*, 4(2):202–210, 1967.

[38] J. N. Lyness. Numerical algorithms based on the theory of complex variable. In *Proceedings of the 1967 22nd national conference*, pages 125–133. ACM, 1967.

[39] W. K. Anderson, J. C. Newman, D. L. Whitfield, and E. J. Nielsen. Sensitivity analysis for Navier-Stokes equations on unstructured meshes using complex variables. *AIAA journal*, 39(1):56–63, 2001.

[40] J. R. R. A. Martins, I. M. Kroo, and J. J. Alonso. An automated method for sensitivity analysis using complex variables. *AIAA paper 2000-0689, 38th Aerospace Sciences Meeting, 2000–0689*, 2000.

[41] J. R. R. A. Martins, P. Sturdza, and J. J. Alonso. The complex-step derivative approximation. *ACM Transactions on Mathematical Software*, 29(3):245–262, 2003.

[42] M. de' Michieli Vitturi and G. Lari. IMEX_SfloW2D v. 1.0.0 (Version 1.0.0), Zenodo.

[43] Abraham Ziv. Relative distance-an error measure in round-off error analysis. *Mathematics of Computation*, 39(160):563–569, 1982.

[44] N. J. Balmforth, R. V. Craster, P. Perona, A. C. Rust, and R. Sassi. Viscoplastic dam breaks and the bostwick consistometer. *Journal of non-Newtonian fluid mechanics*, 142:63–78, 2007.

[45] P. Saramito, C. Smutek, and B. Cordonnier. Numerical modeling of shallow non-Newtonian flows: part I. the 1D horizontal dam break problem revisited. *International journal of numerical analysis & modeling, Series B*, 4:283–298, 2013.

[46] B. Cordonnier, E. Lev, and F. Garel. Benchmarking lava-flow models. *Geological Society, London, Special Publications*, 426:425–445, 2015.

[47] J. R. Lister. Viscous flows down an inclined plane from point and line sources. *Journal of Fluid Mechanics*, 242:631–653, 1992.

[48] R. Lecuna, F. Delgado, A. Ortiz, Fernandez I. Castro, P. B., and C. J. Renedo. Thermal-fluid characterization of alternative liquids of power transformers: a numerical approach. *IEEE Transactions on Dielectrics and Electrical Insulation*, 22(5):2522–2529, 2015.

[49] Y. Wang, K. Hutter, and S. P. Pudasaini. The Savage-Hutter theory: a system of partial differential

equations for avalanche flows of snow, debris, and mud. *ZAMM*, 84(8):507–527, 2004.